Vertical Structure and Scaling of Turbulent Mixing in the Benthic Biolayer of Stream and Coastal Sediments

Stanley B. Grant[1,2], Jesus D. Gomez-Velez[3], Marco Ghisalberti[4], Ian Guymer[5], Fulvio Boano[6], Kevin Roche[7], Judson Harvey[8]

[1]Occoquan Watershed Monitoring Laboratory, Department of Civil and Environmental Engineering, Virginia Tech, 9408 Prince William Street, Manassas VA 20110, USA

[2]Center for Coastal Studies, Virginia Tech, 1068A Derring Hall (0420), Blacksburg, VA 24061, USA

[3]Department of Civil and Environmental Engineering, Vanderbilt University, Nashville, TN 37205, USA

[4]Oceans Graduate School, University of Western Australia, Perth, WA, 6009, Australia.

[5]Department of Civil and Structural Engineering, Sir Frederick Mappin Building, Mappin Street, Sheffield, S1 3JD, England

[6]Department of Environment, Land and Infrastructure Engineering, Politecnico di Torino, Torino 10129, Italy.

[7]Institute of Environmental al Research and Water Research, Spanish National Research Council (CSIC), 08034 Barcelona, Spain

[8]United States Geological Survey, Earth System Processes Division, Reston VA, 20192, USA

Corresponding author: Stanley B. Grant (stanleyg@vt.edu)

Key Points:

- A one-dimensional diffusion model, based on Duhamel's Theorem, is developed for turbulent mass transport in the benthic biolayer
- The model reproduces solute transfer above and below the sediment-water interface provided the diffusivity decays exponentially with depth
- Turbulent mixing increases with the Permeability Reynolds Number, and appears to be driven by turbulent pumping

Abstract

In this paper we develop and test a rigorous modeling framework, based on Duhamel's Theorem, for the unsteady one-dimensional transport and mixing of a solute across a flat sediment-water interface (SWI) and through the benthic biolayer of a turbulent stream. The modeling framework is novel in that it allows for depth-varying diffusivity profiles, accounts for the change in porosity across the SWI and captures the two-way coupling between evolving solute concentrations in both the overlying water column and interstitial fluids of the sediment bed. We apply this new modeling framework to an extensive set of previously published laboratory measurements of turbulent mixing across a flat sediment bed, with the goal of evaluating four diffusivity profiles (constant, exponentially declining, and two hybrid models that account for molecular diffusion and enhanced turbulent mixing in the surficial portion of the bed). The exponentially declining profile is superior (based on RMSE, coefficient of determination, AICc, and model parsimony) and its reference diffusivity scales with a dimensionless measure of stream turbulence and streambed permeability called the Permeability Reynolds Number, Re_K. The diffusivity's dependence on Re_K changes abruptly at $\mathrm{Re}_K = 1$, reflecting different modes of mixing below (dispersion) and above (turbulent diffusion) this threshold value. The depth-scale over which the diffusivity exponentially decays is about equal to the thickness of the benthic biolayer (2 to 5 cm), implying that turbulent mixing, and specifically turbulent pumping, may play an outsized role in the biogeochemical processing of nutrients and other contaminants in stream and coastal sediments.

Plain Language Summary

How far and fast pollutants travel downstream is often conditioned on what happens in a thin veneer of biologically active bottom sediments called the benthic biolayer. However, before a pollutant can be removed in the benthic biolayer it must first be transported across the sediment-water interface and through the interstitial fluids of these surficial sediments. In this paper we investigate, through mathematical modeling and an evaluation of previously published experimental data, the role that water column turbulence plays in transporting solutes into and through the benthic biolayer of streams and coastal sediments.

64 **1 Introduction**

65 Many physical and biological processes in aquatic ecosystems depend on, or are strongly
66 affected by, turbulent fluid motions at the sediment-water interface (SWI) (Franca and
67 Brocchini, 2015; Grant and Marusic, 2011). Stream turbulence drives the vertical
68 transport of dissolved constituents through the water column (Tomasek et al., 2018;
69 O'Connor and Hondzo, 2008; Hondzo, 1998) imposing an upper limit on the rate that
70 reactive constituents, nitrate for example, can be assimilated and removed by the
71 streambed (Grant et al., 2018a). Stream turbulence also facilitates the transport and
72 mixing of dissolved and fine particulate materials and energy across the SWI and in the
73 benthic biolayer, the upper 5 cm of the streambed where much of the microbial biomass,
74 as well as nutrient and pollutant processing, is concentrated (Tomasek et al., 2018; Knapp
75 et al., 2017; Caruso et al., 2017; Trauth et al., 2014; Harvey et al., 2013; Zarnetske et al.,
76 2011; Battin et al., 2008; Dahm et al., 2002).

77 At the scale of the benthic biolayer, stream turbulence facilitates mixing in at least
78 two ways (**Figure 1a**): (1) "turbulent pumping" occurs when spatially coherent eddies
79 spawn pressure waves that travel along the SWI and drive temporally oscillating laminar
80 flow across the interface (Kim et al., 2020; Zhong et al., 2016; Boano et al., 2011;
81 Higashino et al., 2009); and (2) "turbulence penetration" occurs when turbulent eddies
82 drive intermittent transport of mass and momentum across the interface (Kim et al., 2020;
83 Roche et al., 2018; Voermans et al., 2017; Reidenbach et al., 2010; Packman et al., 2004).
84 If ripples and dunes are present on the streambed surface, mixing across the benthic
85 biolayer is also facilitated by the advective transport of solutes across the SWI in spatially
86 isolated upwelling and downwelling zones, "bedform pumping" (Azizian et al., 2018;

87 Grant et al., 2014; Fleckenstein et al., 2010; Cardenas et al., 2008; Elliot and Brooks,
88 1997a,b; Thibodeaux and Boyle, 1987)) and the entrapment and release of interstitial
89 fluids associated with bedform migration, "bedform turnover" (Wolke et al., 2020; Zheng
90 et al., 2019; Elliot and Brooks, 1997a,b)). Solute mixing in the streambed is also
91 controlled by molecular diffusion (which smooths out the steep concentration gradients
92 generated by the above transport mechanisms, Hester et al., 2017), bio-diffusion (in
93 which pore fluids and sediment are "pumped" through benthic macrofauna and plants,
94 Thibodeaux et al., 2011), and the streambed's permeability and porosity fields (which can
95 vary temporally and spatially, Laube et al., 2018; Newcomer et al., 2016; Stewardson et
96 al., 2016; Salehin et al., 2004; Herzog et al., 2018).

97 At present, only under highly idealized experimental or modeling conditions is it
98 possible to resolve the spatially and temporally complex eddy advection pathways
99 generated by the transport mechanisms described above. Due to its simplicity,
100 mathematical tractability and prior agreement with scaling studies, a common alternative
101 is to approximate mass transport across the SWI, and through the benthic biolayer, as a
102 flux-gradient diffusive process (Voermans et al., 2018):

103 $$J(y,t) = -D_{\mathrm{eff}}(y)\frac{\partial(\theta C_s)}{\partial y} \qquad (1a)$$

104 Here, $J(y,t)$ [M L^{-2} T^{-1}] and $C_s(y,t)$ [M L^{-3}] are the horizontally and temporally averaged
105 vertical flux and interstitial solute concentration at depth y [L] and time t [T] in the
106 sediment. The effective diffusivity, D_{eff} [L^2 T^{-1}], for solute mixing in the surficial
107 sediments of a stream or coastal sediment sums over contributions from the tortuosity-
108 modified molecular diffusion, D'_{m} [L^2 T^{-1}], dispersion, D_{d} [L^2 T^{-1}], and turbulent

diffusion, D_t [$L^2\ T^{-1}$] (Roch et al., 2019; Roche et al., 2018; Grant et al., 2018b; Voermans et al., 2018; Voermans et al.,2017; Chandler et al., 2016; Zhong et al., 2016; Boano et al., 2014; Grant et al., 2012; Boano et al., 2011; Grant and Marusic, 2011; Reidenbach et al., 2010; O'Connor and Harvey, 2008; O'Connor and Hondzo, 2008; Packman et al., 2004; Nagaoka and Ohgaki, 1990; Richardson and Parr, 1988):

$$D_{\text{eff}} = D'_m + D_d + D_t \tag{1b}$$

Dispersion arises from spatial correlations between the time-averaged vertical velocity component and the local mean solute concentration, while turbulent diffusion arises from temporal correlations between the turbulent vertical velocity component and the instantaneous turbulent concentration field (Voermans et al., 2018).

The use of equations (1a) and (1b) to describe mixing in the benthic biolayer raises three questions. First, given that the mean flow and shear (turbulence) fields responsible for mixing across the benthic biolayer are damped out with depth by viscous dissipation (He et al., 2019; Roche et al, 2018; Voermans et al., 2017; Pokrajac and Manes, 2009; Bruegem et al., 2006) how should the effective diffusivity be structured vertically, and does the answer depend on the nature of the transport mechanism under consideration (e.g., dispersion or turbulent diffusion)? Second, once an appropriate vertical structure is selected for the effective diffusivity, how well does the flux-gradient diffusive model (equation (1a)) represent solute transport through the streambed? Third, how do we extrapolate effective diffusivities measured in the laboratory to streams and coastal sediments? In this paper we focus on addressing these three questions in the context of turbulent mixing across a flat sediment bed. Complementary efforts are

131 underway to address mixing in the benthic biolayer by bedform pumping and bedform
132 turnover.

133 The paper is organized as follows. In **Section 2** we demonstrate, through an
134 application of Duhamel's Theorem (Perez et al., 2013), that solute concentration in the
135 interstitial fluids of the sediment bed can be represented as the convolution of solute
136 concentration in the water column and a Green's function for mass transport in the
137 interstitial fluids of the streambed (Leij et al., 2000). This starting point leads to a set of
138 explicit solutions, valid for any Green's function, for the spatiotemporal evolution of
139 solute concentration in the water and sediment columns of a closed system. Notably,
140 these solutions capture the two-way coupling of evolving solute concentrations above and
141 below the SWI, whereby mass transfer out of the streambed alters mass concentration in
142 the overlying water column which, in turn, alters mass transfer into the streambed, and so
143 on (**Figure 1b**). We then derive six Green's functions for two choices of the lower
144 boundary condition (finite or semi-infinite sediment domain) and four functional forms of
145 the diffusivity depth profile. In **Section 3** we demonstrate how this theory can be used to
146 simulate unsteady mass transfer in a stirred tank experiment, and in **Section 4** apply it to
147 previously published measurements of turbulent mass transfer across a flat
148 unconsolidated sediment bed in a well-stirred tank (Chandler et al., 2016; Chandler,
149 2012). We address the three questions raised above in **Section 5** and present our
150 conclusions in **Section 6**.

151 [Figure 1 goes about here]

152 **2 Analytical Modeling Framework**

153 **2.1 Governing Equations for Turbulent Mixing in the Benthic Biolayer**

154 Double averaging over the turbulent timescale (e.g., estimated from the ratio of water
155 depth and stream velocity (Pope, 2012)) and the horizontal plane of the SWI, and
156 assuming that streambed porosity does not change appreciably through the benthic
157 biolayer (i.e., the variable θ appearing in equation (1a) is a fixed constant in the upper 5
158 cm or so of the streambed (Knapp et al., 2017)), we obtain the following mass
159 conservation equation for one-dimensional diffusion of a solute through the interstitial
160 fluids of the sediment bed:

161 $$\frac{\partial C_s}{\partial t} = \frac{\partial}{\partial y}\left(D_{\text{eff}}(y) \frac{\partial C_s}{\partial y} \right) \quad (2a)$$

162 Equation (2a) equates the accumulation of mass in a differential horizontal slice of the
163 sediment beneath a turbulent stream (left hand side) to the vertical diffusive transport
164 (right hand side) of a conservative (non-reactive and non-adsorbing) solute (Incropera et
165 al., 2007). The coordinate y increases with depth into the streambed and its origin (at
166 $y=0$) is positioned at the horizontal plane of the SWI (**Figure 1a**).

167 In this study we explore four functional forms of the effective diffusivity depth
168 profile, $D_{\text{eff}}(y) = D_{\text{eff},0} f(y)$, where the variable $D_{\text{eff},0}$ is the surficial effective diffusivity (at
169 the SWI, $y=0$) and $f(y)$ (unitless) is a piecewise continuous function that equals unity at
170 the SWI (i.e., $f(0)=1$). After substituting this functional form for the effective diffusivity,
171 equation (2a) can be rewritten in dimensionless form where the new dependent variable,
172 c_s [-], incorporates the solute's initial concentration in the interstitial pore fluids of the
173 sediment bed and the overlying water column (C_{s0} and C_{w0} [M L^{-3}], respectively):

174 $$\frac{\partial c_s}{\partial \bar{t}} = \frac{\partial}{\partial \bar{y}}\left(f(\bar{y}) \frac{\partial c_s}{\partial \bar{y}} \right) \quad (2b)$$

175 $$c_s(\bar{y},\bar{t}) = \frac{C_s(\bar{y},\bar{t}) - C_{s0}}{C_{w0} - C_{s0}},\ c_s(\bar{y},\bar{t}) \in [0,1] \quad (2c)$$

176 $$\bar{t} = t/t_T \geq 0,\ t_T = 1/\left(D_{\mathrm{eff},0} a^2\right),\ \bar{y} = a y \geq 0 \quad (2d)$$

177 The constant a [L^{-1}] is an inverse depth-scale (the definition of which depends on the
178 choice of diffusivity profile, see later) and t_T is a time constant for solute mixing in the
179 benthic biolayer. Given the definition of the dimensionless concentration group (equation
180 (2c)), the initial condition for equation (2b) becomes:

181 $$c_s(\bar{y},\bar{t}=0) = 0 \quad (3a)$$

182 At the upper boundary (at the SWI, $y = 0$) we require that the interstitial tracer
183 concentration equals the tracer concentration in the overlying water column,
184 $C_s(y=0,t) = C_w(t)$ [M L^{-3}], which depends only on time; i.e., solute concentration in the
185 water column is well-mixed. Expressed in dimensionless form the upper boundary
186 condition becomes:

187 $$c_s(\bar{y}=0,\bar{t}) = \frac{C_w(\bar{t}) - C_{s0}}{C_{w0} - C_{s0}} H(\bar{t}) = c_w(\bar{t}) H(\bar{t}) \quad (3b)$$

188 $$c_w(\bar{t}) = \frac{C_w(\bar{t}) - C_{s0}}{C_{w0} - C_{s0}},\ c_w(\bar{t}) \in [0,1],\ H(\bar{t}) = \begin{cases} 0, & \bar{t} < 0 \\ 1, & \bar{t} > 0 \end{cases} \quad (3c)$$

189 The Heaviside function $H(\bar{t})$ [-] appearing on the righthand side of equation (3b) ensures
190 that the upper boundary condition is zero for $\bar{t} < 0$ (this detail becomes important for the
191 application of Duhamel's Theorem below). By expressing the upper boundary condition
192 in this way, we are assuming that mass transfer across the SWI is rate-limited by the

193 mixing of solute within the streambed and not by convective mixing across the
194 concentration boundary layer above the streambed (Grant et al., 2018). Put another way,
195 we are assuming that the Biot Number—which expresses the ratio of timescales for
196 diffusive mixing in the streambed and convective mass transfer across the turbulent
197 boundary layer above the streambed—is much greater than unity (Incropera et al., 2007).
198 One of two lower boundary conditions can be selected, depending on whether the
199 sediment bed is assumed to be finite (equation (3d)) or semi-infinite (equation (3e)) in
200 extent.

201 $$\left.\frac{\partial c_s}{\partial \overline{y}}\right|_{\overline{y}=\overline{d}_b} = 0 \qquad (3d)$$

202 $$c_s\left(\overline{y} \to \infty, \overline{t}\right) = 0 \qquad (3e)$$

203 Equation (3d) enforces a no-flux boundary condition at scaled depth $\overline{d}_b = a d_b$ [-] where d_b
204 [L] is the depth of the sediment bed (**Figure 1**). Equation (3e) implies that, very deep into
205 the bed ($\overline{y} \to \infty$), the interstitial concentration is maintained at its initial state.

206 **2.2 Duhamel's Theorem and Green's Functions**

207 We seek an explicit solution to the above system of equations that is valid for any time-
208 varying solute concentration in the overlying water column, any piecewise continuous
209 diffusivity profile, and either a finite or semi-infinite streambed. To this end we invoke
210 Duhamel's Theorem, an analytical approach for solving the diffusion equation in cases
211 where one boundary is a piece-wise continuous function of time (Perez Guerrero et al.,
212 2013). Proofs of this theorem typically assume that the diffusion coefficient is constant.
213 However, as demonstrated in the Supplemental Information (**Text S1**), the theorem also
214 applies in cases where the diffusion coefficient varies solely as a function of depth.

For the version of Duhamel's Theorem adopted here, three conditions must be met (Myers, 1971): (1) the system must have a zero initial state; (2) the differential equation and boundary conditions must be homogeneous with the exception of a single time-dependent boundary condition or source/sink term in the differential equation; and (3) the single nonhomogeneous term should be initially equal to zero. By design, our system meets all three requirements. Accordingly, Duhamel's Theorem allows us to express the interstitial solute concentration in the sediment bed as a convolution of the time-derivative of the water column concentration $c_w\left(\bar{t}\right)$ and a so-called *auxiliary function* $c_s^A\left(\bar{y},\bar{t}\right)$ where v is a dummy integration variable (Meyers, 1971):

$$c_s\left(\bar{y},\bar{t}\right)=\int_0^{\bar{t}} c_s^A\left(\bar{y},\bar{t}-v\right)\frac{d}{dv}\left[c_w\left(v\right)H\left(v\right)\right]dv \tag{4a}$$

The auxiliary function is, by definition, a solution to the same system of equations described above for the interstitial solute concentration (equations (2b) - (3e)) but with the nonhomogeneous term replaced by unity (compare equations (3b) and (4d)):

$$\frac{\partial c_s^A}{\partial \bar{t}}=\frac{\partial}{\partial \bar{y}}\left(f\left(\bar{y}\right)\frac{\partial c_s^A}{\partial \bar{y}}\right) \tag{4b}$$

$$c_s^A\left(\bar{y},\bar{t}=0\right)=0,\ \bar{y}\geq 0 \tag{4c}$$

$$c_s^A\left(\bar{y}=0,\bar{t}\right)=H\left(\bar{t}\right) \tag{4d}$$

The auxiliary function's lower boundary condition depends on whether the sediment bed is finite or semi-infinite in extent:

$$\left.\frac{\partial c_s^A}{\partial \bar{y}}\right|_{\bar{y}=\bar{d}_b,\bar{t}}=0 \tag{4e}$$

$$c_s^A\left(\bar{y}\rightarrow\infty,\bar{t}\right)=0 \tag{4f}$$

235 Duhamel's Theorem (equation (4a)) can also be expressed as a convolution of the
236 dimensionless water column concentration, $c_w(\bar{t})$, and a so-called Green's function,
237 $G(\bar{y},\bar{t})$ [T^{-1}], scaled here by the mixing timescale introduced earlier, $\bar{G}(\bar{y},\bar{t})=t_T G(\bar{y},\bar{t})$ (see
238 **Text S2** for details):

239 $$c_s(\bar{y},\bar{t})=\int_0^{\bar{t}} \bar{G}(\bar{y},v)c_w(\bar{t}-v)dv \quad (5a)$$

240 $$\bar{G}(\bar{y},\bar{t})=\frac{\partial c_s^A}{\partial \bar{t}} \quad (5b)$$

241 According to equation (5a), solute concentration in the interstitial fluid of the sediment
242 bed at any depth and time, $c_s(\bar{y},\bar{t})$, depends on the entire prior history of solute
243 concentration in the water column, $c_w(\bar{t})$, filtered through the Green's function, $\bar{G}(\bar{y},\bar{t})$.
244 The Green's function, in turn, is a fundamental solution to the diffusion equation
245 (equation (2b)) that characterizes the response of solute concentration in the interstitial
246 fluids of the streambed to an impulsive injection of mass at the SWI at $\bar{t}=0$, $c_w(\bar{t})=\delta(\bar{t})$,
247 where $\delta(\bar{t})$ [-] is the Dirac Delta function. Because the Green's function is calculated
248 from the auxiliary function (equation (5b)) its functional form will depend on the vertical
249 structure of the diffusivity profile, $f(\bar{y})$, and the lower boundary condition (either
250 equation (4e) or (4f)). Five Green's functions, corresponding to different combinations of
251 the diffusivity profile and lower-boundary condition, are derived in **Section 2.4**.

252 **2.3 Two-Way Coupling Across the SWI in a Closed System**

253 In a typical application of Duhamel's Theorem, the time-dependence of the
254 nonhomogeneous boundary condition is stipulated in advance. In our case, however, the

255 nonhomogeneous boundary condition (i.e., the water column concentration, equation
256 (3b)) depends on mass flux across the SWI through a mass balance over the water
257 column. For a closed system with a well-mixed water column, such as the stirred tank in
258 **Figure 1b**, the water column mass balance takes on the following form:

259 $$A_b h_w \frac{dC_w}{dt} = A_b \theta D_{\text{eff},0} \left.\frac{\partial C_s}{\partial y}\right|_{y=0,t} \quad (6a)$$

260 In this equation, the change of solute mass in the water column (left hand side) equals the
261 rate of mass transfer across the SWI by turbulent mixing (right hand side). New variables
262 appearing here include the interfacial area, A_b [L^2], of the streambed and the height of the
263 water column, h_w [L]. Streambed porosity, θ, is included on the right-hand side of the
264 equation to account for the streambed's porosity; specifically, the abrupt change in area
265 over which solute mass transport occurs above and below the SWI (Grant et al., 2012).
266 Expressing equation (6a) using the dimensionless variables introduced earlier, we obtain
267 equation (6b) where the dimensionless variable, $\overline{h}_w$ (equation (6c)), is a scaled form of
268 the water column depth.

269 $$\frac{dc_w}{d\overline{t}} = \frac{1}{\overline{h}_w} \left.\frac{\partial c_s}{\partial \overline{y}}\right|_{\overline{y}=0,\overline{t}} \quad (6b)$$

270 $$\overline{h}_w = \frac{a h_w}{\theta} \quad (6c)$$

271 Two-way coupling across the SWI manifests mathematically as a dependence of
272 the water column concentration (left hand side, equation (6b)) on the streambed's
273 interstitial solute concentration (right hand side, equation (6b)) and, simultaneously, the
274 dependence of the streambed's interstitial solute concentration (left hand side, equation
275 (5a)) on the solute concentration in the water column (through its convolution with the

276 Green's function, right hand side equation (5a)). This two-way coupling can be solved
277 exactly by manipulating the water and sediment mass balance equations in the Laplace
278 Domain. As demonstrated in Supplemental Information (**Text S3**), the result is a set of
279 fully coupled solutions for solute concentration in the water and sediment columns of a
280 closed system with two-way coupling across the SWI "turned on":

281 $$C_w\left(\overline{t}\right)=\left(C_{w0}-C_{s0}\right)\mathcal{L}^{-1}\left[\frac{1/\overline{s}}{1-\frac{1}{\overline{s}\overline{h}_w}\left(\partial\tilde{G}/\partial\overline{y}\right)_{\overline{y}=0,\overline{s}}}\right]+C_{s0} \quad (7a)$$

282 $$C_s\left(\overline{y},\overline{t}\right)=\left(C_{w0}-C_{s0}\right)\mathcal{L}^{-1}\left[\frac{\tilde{G}\left(\overline{y},\overline{s}\right)/\overline{s}}{1-\frac{1}{\overline{s}\overline{h}_w}\left(\partial\tilde{G}/\partial\overline{y}\right)_{\overline{y}=0,\overline{s}}}\right]+C_{s0} \quad (7b)$$

283 In these solutions, the symbol $\mathcal{L}^{-1}\left[\bullet\right]$ represents the inverse Laplace Transform, $\overline{s}=st_{\mathrm{T}}$ [-]
284 is a dimensionless form of the Laplace Transform variable s [T^{-1}], and $\tilde{G}$ is the Laplace
285 transform of the dimensionless Green's function which, in turn, depends on the
286 diffusivity depth profile $f\left(\overline{y}\right)$ and bottom boundary condition (through the solution to the
287 auxiliary function (equation (5b)). A corresponding set of solutions can also be derived
288 for when two-way coupling across the SWI is "turned off"; i.e., the diffusion equation's
289 upper boundary condition is held at its initial state, $C_s\left(\overline{y}=0,\overline{t}\right)=C_{w0}$:

290 $$C_w\left(\overline{t}\right)=\left(C_{w0}-C_{s0}\right)\mathcal{L}^{-1}\left[\frac{1}{\overline{s}}\left(\frac{1}{\overline{s}\overline{h}_w}\left.\frac{\partial\tilde{G}}{\partial\overline{y}}\right|_{\overline{y}=0,\overline{s}}+1\right)\right]+C_{s0} \quad (7c)$$

291 $$C_s\left(\overline{y},\overline{t}\right)=\left(C_{w0}-C_{s0}\right)\mathcal{L}^{-1}\left[\frac{\tilde{G}\left(\overline{y},\overline{s}\right)}{\overline{s}}\right]+C_{s0} \quad (7d)$$

292 [Figure 2 goes about here]

293 Depending on the choice of Green's function, the inverse Laplace transforms appearing
294 in equations (7a) - (7d) were either determined analytically, or numerically evaluated
295 using Gaussian Quadrature implemented in the Mathematica package authored by U.
296 Graf (Graf, 2004).

297 **2.4 Laplace Domain Solutions for the Green's Function**

298 In **Table 1** we present five Laplace domain solutions for the Green's function given four
299 different choices of the diffusivity depth profile and two different choices of the bottom
300 boundary condition (finite or semi-infinite sediment bed) (derivations in Supplemental
301 Information**, Text S4)**. Together with equations (7a) through (7d), these five Green's
302 functions provide a total of 20 different solution combinations for solute concentration in
303 the water and sediment column of a closed system with two-way coupling across the SWI
304 turned on (equations (7a) and (7b)) or off (equations (7c) and (7d)). The four diffusivity
305 depth profiles we evaluated include (**Figure 2**): (1) constant (*C Profile*, equation (8a));
306 (2) exponentially declining (*E Profile*, equation (8b)); (3) exponentially declining to a
307 tortuosity-modified molecular diffusion coefficient (*E2M Profile*, equation (8c)); and (4)
308 constant to exponentially declining diffusivity (*C2E Profile*, equation (8d)).

309 $$f_{\mathrm{C}}\left(\overline{y}\right)=1,\ \overline{y}=a_{\mathrm{C}}y \tag{8a}$$

310 $$f_{\mathrm{E}}\left(\overline{y}\right)=e^{-\overline{y}},\ \overline{y}=a_{\mathrm{E}}y \tag{8b}$$

311 $$f_{\mathrm{E2M}}\left(\overline{y}\right)=\begin{cases} e^{-\overline{y}},\ 0\le\overline{y}\le\overline{\ell}_m \\ \overline{D}=D'_{\mathrm{m}}/D^{\mathrm{E2M}}_{\mathrm{eff},0},\ \overline{y}>\overline{\ell}_m \end{cases},\ \overline{\ell}_m=-\ln\overline{D},\ 0<\overline{D}<1,\ \overline{y}=a_{\mathrm{E2M}}y \tag{8c}$$

312 $$f_{\mathrm{C2E}}\left(\overline{y}\right)=\begin{cases} 1,\ 0\le\overline{y}\le\overline{\ell}_{\mathrm{t}} \\ e^{-\left(\overline{y}-\overline{\ell}_{\mathrm{t}}\right)},\ \overline{y}>\overline{\ell}_{\mathrm{t}} \end{cases},\ \overline{\ell}_t=a_{\mathrm{C2E}}\ell_t,\ \overline{y}=a_{\mathrm{C2E}}y \tag{8d}$$

313 Most laboratory (Marion and Zaramella, 2015; O'Connor and Harvey, 2008; Grant et al.,
314 2012) and field (Wörman, 2000) studies of diffusive mixing across the SWI adopt the C
315 Profile. However, several studies (He et al., 2019; Roche et. al, 2019; Chandler et al.,
316 2016; Nagaoka and Ohgaki, 1990) have shown that turbulent mixing in the sediment bed
317 declines exponentially with depth, and a recent numerical modeling study concluded that
318 the E Profile is consistent with experimental breakthrough curves measured in the
319 laboratory and field (Bottacin-Busolin, 2019). The E2M profile is a natural extension of
320 the E Profile that accounts for the fact that the tortuosity-modified molecular diffusion
321 coefficient D'_m [L^2 T^{-1}] imposes a lower-bound on the effective diffusivity. E2M's
322 mathematical representation (equation (8c)) includes two new variables: the
323 dimensionless depth at which the diffusivity profile transitions from exponentially
324 declining to the tortuosity-modified molecular diffusion coefficient, $\overline{\ell}_m = a_{\mathrm{E2M}}\ell_m$ [-] where
325 ℓ_m [L] is the transition depth and $\overline{D} = D'_m / D^{\mathrm{E2M}}_{\mathrm{eff},0}$ [-] is a dimensionless form of the
326 tortuosity-modified molecular diffusion coefficient. These two parameters are
327 mathematically related as follows: $\overline{\ell}_m = -\ln \overline{D}$. Finally, the C2E Profile captures enhanced
328 mixing at the top of the streambed by extending the surficial effective diffusivity $D^{\mathrm{C2E}}_{\mathrm{eff},0}$ to
329 a depth $y = \ell_t$ [L] below the SWI. For depths greater than the constant mixing thickness,
330 $y > \ell_t$, the diffusivity profile declines exponentially. The dimensionless form of the
331 enhanced mixing thickness ℓ_t is defined in the usual way, $\overline{\ell}_t = a_{\mathrm{C2E}}\ell_t$.

332 [Table 1 goes about here]

333 **3 Example of the Theory's Application to Mixing Across the SWI in a Stirred Tank**

334 As a tangible example of the theory presented in **Section 2**, consider an experiment
335 (along the lines examined in detail later, see **Section 4**) in which a mass M of a
336 conservative solute is added to the interstitial fluids of a sediment bed in an otherwise
337 solute-free stirred tank. Adopting the notation indicated in **Figure 1b**, the initial
338 interstitial solute concentration in the sediment bed will be: $C_{s0} = M/\left(d_b A_b \theta\right)$. At time $t = 0$
339 the impeller is turned on causing solute concentration in the overlying water column to
340 increase as solute turbulently mixes out of the bed. If the experiment runs long enough,
341 the solute concentration in the water column and interstitial fluids of the sediment bed
342 will approach a final (well-mixed) equilibrium concentration, C_{eq} [M L^{-3}]:

343 $$\frac{C_{eq}}{C_{s0}} = \frac{\overline{d}_b}{1+\overline{d}_b},\ \overline{d}_b = d_b \theta / h_w \qquad (9a)$$

344 How does solute concentration in the overlying water column and interstitial fluids of the
345 sediment bed evolve from their initial state (where all solute mass is located in the
346 sediment bed) to the final (well-mixed) state given by equation (9a)? Within the context
347 of our modeling framework, the answer depends on the depth-dependence of the
348 diffusivity profile, whether two-way coupling across the SWI is turned "on" or "off", and
349 whether the sediment bed is assumed to be semi-infinite or finite in extent.

350 As an illustration we adopt the C Profile and derive from the theoretical
351 framework in **Section 2** the following three explicit solutions for the evolution of solute
352 concentration in the water column (see **Text S5** for details): (1) a "null model" which
353 assumes two-way coupling across the SWI is turned off and the sediment bed is infinitely
354 deep (equation (9b)); (2) an "infinite bed" model that assumes two-way coupling is
355 turned on and the sediment bed is infinitely deep (equation (9c)); and (3) a "finite bed"

model that accounts for both two-way coupling across the SWI and the finite depth of the sediment bed (equation (9d)).

$$\frac{C^{\mathrm{C}}_{w,\mathrm{null}}\left(\overline{t}_{\mathrm{C}}\right)}{C_{s0}} = 2\sqrt{\frac{\overline{t}_{\mathrm{C}}}{\pi}}\ ,\ \overline{t}_{\mathrm{C}} = \theta^2 D^{\mathrm{C}}_{\mathrm{eff},0} t \big/ h_w^2 \tag{9b}$$

$$\frac{C^{\mathrm{C}}_{w,\infty}\left(\overline{t}_{\mathrm{C}}\right)}{C_{s0}} = 1 - e^{\overline{t}_{\mathrm{C}}}\mathrm{erfc}\left(\sqrt{\overline{t}_{\mathrm{C}}}\right) \tag{9c}$$

$$\frac{C^{\mathrm{C}}_{w,\mathrm{finite}}\left(\overline{t}_{\mathrm{C}}\right)}{C_{s0}} = 1 - \mathcal{L}^{-1}\left[\frac{1/\overline{s}}{1+\tanh\left(\overline{d}_b\sqrt{\overline{s}}\right)\big/\sqrt{\overline{s}}}\right] \tag{9d}$$

The corresponding set of solutions for solute concentration in the interstitial fluids of the sediment bed are as follows:

$$\frac{C^{\mathrm{C}}_{s,\mathrm{null}}\left(\overline{y}_{\mathrm{C}},\overline{t}_{\mathrm{C}}\right)}{C_{s0}} = \mathrm{erfc}\left(\frac{\overline{y}_{\mathrm{C}}}{\sqrt{4\overline{t}_{\mathrm{C}}}}\right),\ \overline{y}_{\mathrm{C}} = \theta y / h_w \tag{10a}$$

$$\frac{C^{\mathrm{C}}_{s,\infty}\left(\overline{y}_{\mathrm{C}},\overline{t}_{\mathrm{C}}\right)}{C_{s0}} = 1 - e^{\overline{t}_{\mathrm{C}}+\overline{y}_{\mathrm{C}}}\mathrm{erfc}\left(\frac{2\overline{t}_{\mathrm{C}}+\overline{y}_{\mathrm{C}}}{\sqrt{4\overline{t}_{\mathrm{C}}}}\right) \tag{10b}$$

$$\frac{C^{\mathrm{C}}_{s,\mathrm{finite}}\left(\overline{y}_{\mathrm{C}},\overline{t}_{\mathrm{C}}\right)}{C_{s0}} = 1 - \mathcal{L}^{-1}\left[\frac{\cosh\left(\left(\overline{d}_b-\overline{y}_{\mathrm{C}}\right)\sqrt{\overline{s}}\right)}{\overline{s}\cosh\left(\overline{d}_b\sqrt{\overline{s}}\right)+\sqrt{\overline{s}}\sinh\left(\overline{d}_b\sqrt{\overline{s}}\right)}\right] \tag{10c}$$

The superscript "C" indicates that these solutions are specific to the C Profile.

The null model predicts that solute concentration in the water column increases without bound and in proportion to the square root of time (i.e., solute concentration in the water column increases linearly when plotted against $\sqrt{\overline{t}_{\mathrm{C}}}$, thick black dashed line, **Figure 3a**). The infinite bed model rises with the null model initially (i.e., until around $\sqrt{\overline{t}_{\mathrm{C}}} \approx 0.25$) but then slows as two-way coupling reduces the rate of mass transfer across the SWI (thin black solid curve in **Figure 3a**). The finite bed model exhibits three phases

373 (colored dashed lines in the figure): tracking the null solution early on, transitioning to
374 the infinite bed solution at intermediate times, and stabilizing at a final equilibrium
375 concentration at long times (thin horizontal colored lines).
376 [Figure 3 goes about here]
377 Similar patterns are evident for model-predicted solute concentration in the
378 interstitial fluids of the streambed (**Figure 3b**). For these simulations we focused on the
379 temporal evolution of interstitial solute concentration in the shallow portion of the bed,
380 $\overline{y}_C = 0.05$; this particular depth was chosen so that we would not violate the inequality
381 requirement, $\overline{y}_C \le \overline{d}_b$, for the smallest dimensionless bed depth of $\overline{d}_b = 0.1$ (light blue
382 horizontal lines in **Figure 3**). The null model (thick black dashed curve) predicts a steep
383 drop in solute concentration initially (as solute in the upper portion of the streambed
384 mixes into a solute-free water column) followed by a gradual decline with time (as solute
385 from deeper in the bed mixes upward). The infinite bed solution (thin black curve)
386 declines with the null model initially, but then rebounds as two-way coupling slows mass
387 transfer across the SWI. Indeed, this rebound closely approximates the rise in water
388 column concentration predicted by the infinite bed model (compare thin black curves in
389 **Figures 3a** and **3b**) implying that, when two-way feedback is turned on, solute
390 concentrations in the interstitial fluids near the top of the sediment bed are similar to the
391 solute concentration in the overlying water column. Interstitial solute concentrations
392 predicted by the finite bed model (colored dashed curves in **Figure 3b**) exhibit the same
393 three phases noted above for the water column; namely, they track the null model at early
394 times, follow the infinite bed model at intermediate times, and stabilize at an equilibrium
395 concentration at long times. For the model-data comparisons described in the next section

396 we employ a set of infinite bed models derived for each of the four diffusivity profiles (C,
397 E, E2M, and C2E) and restrict the experimental time window to well before the onset of
398 equilibrium conditions.

399 4 Applying the Theory to Previously Published Measurements

400 4.1 Chandler et al.'s Experiments

401 Next we turn to an extensive set of previously published measurements of turbulent
402 mixing of a conservative tracer (Rhodamine WT) across the SWI in a stirred tank with a
403 flat sediment bed, along the lines of the experimental set-up illustrated in **Figure 1b**
404 (Chandler et al., 2016; Chandler, 2012). Chandler et al.'s study is notable for several
405 reasons. First, it is one of the few where tracer concentrations were simultaneously
406 measured in the water and sediment columns allowing us to directly compare mixing
407 parameters estimated from data collected exclusively above or below the SWI. Second,
408 the twenty (out of twenty-six total) Chandler et al. experiments included in this study
409 cover a range of bed shear velocities ($u_* =$ 0.01 to 0.04 m s^{-1}), mean grain diameters ($d_g =$
410 0.15 to 5.00 mm), and sediment permeabilities ($K =$ 0.18 to 223 m^2). Finally, by
411 conceptually dividing the sediment bed into a series of layers and fitting the diffusion
412 equation (with a constant diffusivity profile) to each layer separately, Chandler et al.
413 concluded that the diffusivity declines exponentially with depth. Nagaoka and Ohgaki
414 (1990), who pioneered this approach, reached a similar conclusion. Thus, there is already
415 a strong indication that the diffusivity in their system declines with depth. One caveat is
416 that Chandler et al.'s range of shear velocities is on the low side for some streams; e.g.,
417 the 72 headwater streams included in the U.S. Lotic Intersite Nitrogen eXperiment (LINX
418 II) had shear velocities ranging from 0.02 to 0.48 m s^{-1} and only seven streams had shear

velocities in the range interrogated by Chandler et al. (Hall et al., 2009). However, when the shear velocity and permeability for each of Chandler et al.'s experiments are combined to calculate a Permeability Reynolds Number, this master variable spans both dispersive and turbulent diffusive mixing regimes (see **Section 5.1**).

Details of Chandler et al.'s experiments and the approach we used for parameter estimation and model performance evaluation are briefly described here (see **Text S6** for details). In brief, the sediment column, which had a depth of $d_b = 0.2$ m and a porosity of $\theta =$ 0.38 to 0.39, consisted of randomly packed single-sized spherical soda glass spheres. In all experiments, the initial state was a Rhodamine WT saturated sediment bed (concentration of $C_{s0} = 100$ ppb) and a Rhodamine-free water column ($C_{w0} =$ 0 ppb) although the actual concentrations varied somewhat by experiment (**Table S1**). Experiments were initiated when the impeller motor was turned on, whereupon tracer concentrations were fluorometrically monitored in the water column and at 5 depths in the sediment column ($x =$ 0.015, 0.049, 0.083, 0.117, and 0.151 m below the SWI) at a frequency of 0.1 Hz over a period of hours to days. Diffusivity profile parameters were inferred by minimizing the root mean squared error (RMSE) calculated from observations and profile-specific infinite bed model predictions using the non-linear least squares algorithms implemented within the "NonlinearModelFit" command in the Mathematica computing package (v. 11.20, Wolfram Research, Inc.). Several model performance metrics were also generated, including RMSE, coefficient of determination (R^2 value), and the corrected Akaike Information Criterion (AICc). The latter was used to rank the performance of the four diffusivity profile models, accounting for the trade-off between model fit and model complexity. The top-ranked (most parsimonious) model has

442 the smallest AICc value (Aho et al., 2014). Because model predictions were based on
443 "infinite bed models" specific to each profile (see **Section 3**), we restricted the
444 experimental window to periods when the bottom interstitial Rhodamine WT
445 concentration, as measured by the deepest probe, was within 90% of its initial value (see
446 t_{final} values in **Table S1**). By this approach, diffusivity profile parameters were estimated
447 for all four diffusivity profiles (C, E, E2M, and C2E) and for 20 of Chandler et al.'s
448 experiments (inferred parameter values, estimated errors, and model performance metrics
449 are summarized in **Tables S2-S7**); six experiments were excluded due to missing data or
450 other issues.

451 **4.2 Experimental Evaluation of the C Profile**

452 Significant bias is evident when tracer concentrations predicted by the C Profile's infinite
453 bed model are compared to Chandler et al.'s experimental data (**Figure 4a**). In this figure
454 we have plotted Chandler et al.'s Rhodamine WT measurements against the square root
455 of dimensionless time, $\sqrt{\bar{t}_{\text{C}}} = \sqrt{t/t_{\text{C}}}$, where the time-constant, $t_{\text{C}} = h_w^2 \big/ \left(\theta^2 D_{\text{eff},0}^{\text{C}}\right)$, varies from
456 experiment-to-experiment depending on the inferred value of the C Profile's effective
457 diffusivity (summarized in **Table S2**); the other two parameters, h_w and θ, varied little
458 across Chandler et al.'s twenty experiments. When plotted in this way Chandler et al.'s
459 data can be compared directly to a single model-predicted curve for the time evolution of
460 Rhodamine WT concentration in the water column (solid black curve, equation (9c), top
461 panel in **Figure 4a**) and at two depths (15 or 151 mm below the SWI) in the sediment
462 column (solid black curves, equation (10b), bottom panel in **Figure 4a**). For clarity,
463 Rhodamine WT measurements at the three intermediate depths (4.9, 8.3, and 117 cm

464 below the SWI) were not included this figure, although these data were included in the
465 model optimization studies described in **Section 5.1**.
466 [Figure 4 goes about here]
467 By virtue of the way Chandler et al.'s experiments were conducted, the
468 Rhodamine WT concentration in the water column is proportional to the cumulative
469 Rhodamine WT mass transferred from the sediment bed to the water column over time.
470 The results plotted in the top panel of **Figure 4a** therefore imply that the C Profile model
471 under- and over-estimates mass transfer out of the sediment bed at short and long times,
472 respectively. A comparison of model-predicted and measured Rhodamine WT
473 concentrations in the sediment bed reveals the problem (bottom panel, **Figure 4a**): the C
474 Profile model under-estimates mixing in the surficial portion of the bed at early times
475 (i.e., predicted concentrations exceed measured concentrations at 15 mm below the SWI)
476 and over-estimates mixing deeper in the bed at later times (i.e., predicted concentrations
477 are less than measured concentrations at 151 mm below the SWI).

478 **4.3 Experimental Evaluation of the E Profile**

479 The model bias described above is reduced substantially when the effective diffusivity
480 decays exponentially with depth (**Figure 4b**). The E Profile's infinite bed model was
481 constructed by substituting its Green's function (equation (T3)) into the water and
482 sediment mass balance solutions (equations (7a) and (7b)) for a closed system with two-
483 way coupling across the SWI "turned on" (the superscript "E" indicates that these
484 solutions are specific to the E Profile):

485 $$C^{E}_{w,\infty}\left(\overline{t}_{\mathrm{E}}\right)=\left(C_{w0}-C_{s0}\right)\mathcal{L}^{-1}\left[\frac{\overline{h}_{w}K_{1}\left(2\sqrt{\overline{s}}\right)}{\overline{s}\overline{h}_{w}K_{1}\left(2\sqrt{\overline{s}}\right)+\sqrt{\overline{s}}K_{0}\left(2\sqrt{\overline{s}}\right)}\right]+C_{s0} \quad (11a)$$

$$C^{E}_{s,\infty}\left(\overline{y},\overline{t}_{\mathrm{E}}\right)=\left(C_{w0}-C_{s0}\right)\mathcal{L}^{-1}\left[\frac{\overline{h}_{w}\sqrt{e^{\overline{y}}}K_{1}\left(2\sqrt{e^{\overline{y}}\overline{s}}\right)}{\overline{s}\overline{h}_{w}K_{1}\left(2\sqrt{\overline{s}}\right)+\sqrt{\overline{s}}K_{0}\left(2\sqrt{\overline{s}}\right)}\right]+C_{s0} \tag{11b}$$

$$\overline{t}_{\mathrm{E}}=t/t_{\mathrm{E}}\ ,\ t_{\mathrm{E}}=1/\left(a_{\mathrm{E}}^{2}D^{\mathrm{E}}_{\mathrm{eff},0}\right)\ ,\ \overline{h}_{w}=a_{\mathrm{E}}h_{w}/\theta\ ,\ \overline{y}=a_{\mathrm{E}}y \tag{11c}$$

Because the E Profile model has two unknown parameters ($D^{\mathrm{E}}_{\mathrm{eff},0}$ and a_{E}, as opposed to the C Profile's one unknown parameter, $D^{\mathrm{C}}_{\mathrm{eff},0}$) there is no longer a single "master" curve against which all of Chandler et al.'s water column data, for example, can be compared to (as there was for the C Profile in the top panel of **Figure 4a**). Instead, for the E Profile (and the C2E Profile described below) model-data comparisons must be conducted on an experiment-by-experiment basis. In **Figure 4b** we therefore focus our model-data comparison on a typical experiment (red symbols in the figure, experiment ID #20110613). To generate model predictions for this experiment we: (1) fit equation (11a) to the experiment's water column data yielding estimates for the inverse depth-scale and effective diffusivity ($a_{\mathrm{E}}=50\pm1.2$ m^{-1} and $D^{\mathrm{E}}_{\mathrm{eff},0}=\left(5.6\pm0.5\right)\times10^{-6}$ m^{2} s^{-1}); and (2) plotted the model against the same abscissa used in **Figure 4a** after applying the following dimensionless time transformation, $\overline{t}_{\mathrm{E}}=\left(\overline{h}_{w}^{2}D^{\mathrm{E}}_{\mathrm{eff},0}/D^{\mathrm{C}}_{\mathrm{eff},0}\right)\overline{t}_{\mathrm{C}}$, and substituting experiment-specific values for the dimensionless water depth ($\overline{h}_{w}=a_{\mathrm{E}}h_{w}/\theta=33\pm14$) and the C Profile's effective diffusivity ($D^{\mathrm{C}}_{\mathrm{eff},0}=\left(3.4\pm0.2\right)\times10^{-7}$ m^{2} s^{-1}). Equation (11a) closely reproduces the experiment's water column concentrations of Rhodamine WT (compare solid curve and red points in **Figure 4b**, top panel), although some model bias is evident for $\sqrt{\overline{t}_{\mathrm{C}}}<0.05$. The E Profile's infinite bed model (equation (11b)) also captures the fast and slow mixing of Rhodamine WT out of the shallow and deep portions of the sediment bed (compare

black curves and red points, lower panel, **Figure 4b**). The last result is notable given that the parameter values used to generate these predictions were inferred from the water column data; i.e., by fitting the E Profile's infinite bed model to measurements of Rhodamine WT in the water column we can predict the evolution of Rhodamine WT in the interstitial fluids of the sediment bed with reasonable fidelity.

4.4 Experimental Evaluation of the E2M Profile

Setting the tortuosity-modified molecular diffusion coefficient, D'_m, as a lower bound on the effective diffusivity does not improve the E Profile's model performance. We arrived at this conclusion by estimating a tortuosity-modified diffusion coefficient for Chandler et al.'s experiments ($D'_m = 1.31\times10^{-10}$ m^{2}s^{-1}) from the ratio of the molecular diffusion coefficient for Rhodamine in water at 21°C ($D_m = 2.9\times10^{-10}$ m^{2}s^{-1}) (Chandler 2012) and the tortuosity of the sediment bed ($\tau = 2.22$), estimated by substituting the measured bed porosity ($\theta = 0.39$) into an empirical formula proposed by Iversen and Jorgensen (1992) for sandy beds: $\tau = 1+2\left(1-\theta\right)$. Values of the inverse depth-scale and effective diffusivity, a_{E2M} and $D_{\mathrm{eff},0}^{\mathrm{E2M}}$, were then inferred by fitting the E2M Profile's infinite bed model (constructed by substituting equations (T5a,b,c) in **Table 1** into equations (7a) and (7b)) to Chandler et al.'s water column Rhodamine WT measurements. Repeating this process for all twenty of Chandler et al.'s experiments reveals that the E2M's inverse depth-scales and effective diffusivities are nearly identical to those inferred from the E Profile model (**Figure S1**, also compare **Tables S4** and **S6**), implying that these two profiles are functionally equivalent. This result can be rationalized by noting that the timescale for mixing through the sediment column by molecular diffusion ($t_{\mathrm{m}} = \ell_{\mathrm{m}}^2 / D'_{\mathrm{m}} \approx 11$ months,

where the mixing depth is $\ell_m = -\ln\left(D'_{\mathrm{m}} / D^{\mathrm{E2M}}_{\mathrm{eff},0}\right) \Big/ a_{\mathrm{E2M}}$, see equation (8c) and discussion thereof) is much longer than the time period Chandler et al. conducted their experiments (days to weeks). While the E2M Profile did not add value (relative to the E Profile) to our analysis of Chandler et al.'s experiments, it might prove useful in settings with very low levels of turbulence and relatively impermeable sediments (i.e., very small values of the Permeability Reynolds Number, see **Section 5**).

4.5 Experimental Evaluation of the C2E Profile

The C2E Profile's infinite bed model provides a near perfect representation of Chandler et al.'s water column data (**Figure 4c**). The C2E's infinite bed model was constructed by substituting its Green's function (equations (T6a) - (T6c) in **Table 1**) into equations (7a) and (7b). We then followed the same two-step procedure outlined in **Section 3.3**, by (1) fitting the model to Rhodamine concentrations measured in the water column during Exp ID# 20110613 ($D^{\mathrm{C2E}}_{\mathrm{eff},0} = \left(1.5 \pm 0.07\right) \times 10^{-6}\ \mathrm{m^2\ s^{-1}}$, $\ell_t = 0.04 \pm 0.002$ m, $a_{\mathrm{C2E}} = 66 \pm 3.1\ \mathrm{m^{-1}}$); and (2) plotting the model against the same abscissa used in **Figures 4a,b** after applying the following dimensionless time transformation, $\overline{t}_{\mathrm{C2E}} = \left(\overline{h}_w^2 D^{\mathrm{C2E}}_{\mathrm{eff},0} / D^{\mathrm{C}}_{\mathrm{eff},0}\right) \overline{t}_{\mathrm{C}}$, and substituting experiment-specific values for the dimensionless water depth ($\overline{h}_w = a_{\mathrm{C2E}} h_w / \theta = 44 \pm 19$) and the C Profile's effective diffusivity ($D^{\mathrm{C}}_{\mathrm{eff},0} = \left(3.4 \pm 0.2\right) \times 10^{-7}\ \mathrm{m^2\ s^{-1}}$). As noted above, the C2E Profile's infinite bed model provides a near perfect match to Rhodamine WT concentrations measured in the water column (compare solid curve and red points in **Figure 4c**). However, when these same parameter values are used to estimate Rhodamine WT concentration in the interstitial fluids of the bed, there is some loss of model performance compared to the E Profile; i.e., the C2E model systematically

underestimates mixing in the streambed, especially for Rhodamine measurements at 15 mm below the SWI (compare lower panels in **Figures 4b** and **4c**).

5. Discussion

Here we expand our focus to include all twenty of Chandler et al.'s experiments with the goal of answering the three questions raised in **Section 1**.

5.1 How is the Effective Diffusivity Structured Vertically?

From refractive index matched particle image velocimetry (RIM-PIV) studies of turbulent motions across the SWI of a permeable streambed, Voermans et al. (2017) concluded that the flux of mass and momentum is dominated by different transport mechanisms (molecular diffusion, dispersion, turbulent diffusion) depending on the magnitude of the Permeability Reynolds Number, $\mathrm{Re}_K = u_* \sqrt{K} / \upsilon$, a dimensionless arrangement of the shear velocity u_* [L T^{-1}], sediment bed permeability K [L^2], and kinematic viscosity of water υ [L^2 T^{-1}]. Specifically, molecular diffusion dominates mixing across the SWI for small values of this dimensionless number ($\mathrm{Re}_K < 0.01$), dispersion for intermediate values ($0.01 < \mathrm{Re}_K < 2$), and turbulent diffusion for large values ($\mathrm{Re}_K > 2$).

Chandler et al.'s dataset allows us to quantitatively compare the performance of the three diffusivity profiles (C, E, and C2E) over a Permeability Reynolds Number range (0.2 to 4.34) that spans dispersive and turbulent diffusive mixing regimes (note that the E2M profile is not included in this list because, as noted in **Section 4.4**, this profile is functionally equivalent to the E Profile in the context of Chandler et al.'s dataset). Based on our earlier analysis of Chandler et al.'s Exp ID 20110613 we concluded that the E Profile represents a substantial improvement over the C Profile (**Section 4.3**). This

573 conclusion extends to the rest of Chandler et al.'s experiments as well (compare blue and
574 red circles in **Figure 5**, inferred parameter values summarized in **Tables S2** – **S5**). In all
575 cases, the E Profile's infinite bed model captures a larger fraction of data variance ($R^2 >$
576 99.5%, **Figure 5a**) and has substantially smaller RMSE values (**Figures 5b**). The E
577 Profile's AICc is also >10 units lower than the C Profile's AICc (**Figure 5c**) implying
578 that, despite its increased complexity (i.e., the C and E Profiles have one and two
579 unknown parameters, respectively) the E Profile is the more parsimonious model (Weijs
580 and Ruddell, 2020; Aho et al., 2014).

581 [Figure 5 goes about here]

582 The C2E Profile's infinite bed model also performs quite well, but is a problem
583 with the inferred values of its inverse depth-scale. Compared to the E Profile, the C2E
584 Profile's infinite bed model has consistently lower RMSE and AICC values (compare
585 crosses and red circles in **Figures 5b** and **5c**) and a slightly improved coefficient of
586 determination ($R^2 > 99.8\%$, **Figure 5a**). However, these improvements come at the cost of
587 a new parameter (the C2E's inverse depth scale, a_{C2E}) whose inferred values are poorly
588 constrained (coefficient of variation in excess of 40 for some experiments, see **Table S7**),
589 highly variable (varying over 1000-fold from experiment-to-experiment, see distribution
590 of values represented by the violin plot in **Figure 6a**) and, in some cases, not physically
591 meaningful (e.g., the implied depth over which the effective diffusivity decays for $y > \ell_t$
592 is $1/a_{\mathrm{C2E}} \approx$ 20 microns for the largest value of a_{C2E} indicated in **Figure 6a**). Inferred
593 values of the C2E Profile's other two parameters (effective diffusivity, $D_{\mathrm{eff},0}^{\mathrm{C2E}}$, and depth of
594 constant mixing, ℓ_t) are strongly correlated ($R^2 = 0.93$ and 0.76) with the effective

595 diffusivity, $D_{\mathrm{eff},0}^{\mathrm{E}}$, and decay length-scale, $1/a_{\mathrm{E}}$, inferred from the E Profile (**Figure 6b**,
596 **6c**), implying that both models capture the same basic information about the vertical
597 structure of the effective diffusivity; namely that the diffusivity is larger at the SWI and
598 lower at depth. In summary, of the four profiles evaluated in this study and across the full
599 range of Permeability Reynolds Numbers evaluated here (including dispersive and
600 turbulent diffusive transport regimes, see horizontal axis of **Figure 5**) the E Profile is the
601 most parsimonious descriptor of the effective diffusivity's vertical structure.
602 [Figure 6 goes about here]

603 **5.2 Is the Flux-Gradient Diffusive Model an Accurate Representation of Turbulent**
604 **Solute Transport Through the Streambed?**

605 We have already shown that the E Profile's infinite bed model captures a large
606 percentage of the variance in Chandler et al.'s water column Rhodamine measurements
607 ($R^2 > 99.5\%$**, Figure 5a**) but this assessment is based on the same datasets used for model
608 calibration. A more rigorous test of the E Profile in particular, and the flux-gradient
609 diffusive model more generally, can be stated as follows: *are the same E Profile*
610 *parameter values obtained when the model is optimized with Rhodamine measured in the*
611 *water column versus when the model is optimized with Rhodamine measured in the*
612 *interstitial fluids of sediment bed?* Put another way, can the evolution of solute
613 concentrations in the interstitial fluids of the sediment bed be inferred from the evolution
614 of solute concentration in the water column, and vice versa?

615 The answer is a qualified "yes". Across all 20 of Chandler et al.'s experiments,
616 effective diffusivities $D_{\mathrm{eff},0}$ estimated from the water and sediment column data are
617 strongly correlated over a 1000-fold change in the magnitude of this parameter (**Figure**

618 **7a,** Pearson's correlation coefficient, $R = 0.867$). Values of the inverse depth-scale
619 inferred from the water and sediment column data are much less variable and not
620 significantly correlated (**Figure 7b**), but their respective log-means ($a = 10^{1.61 \pm 0.18}$ m^{-1} and
621 $a = 10^{1.70 \pm 0.08}$, respectively) are equal within error. The corresponding mean values
622 ($a_E = 44.0 \pm 18.5$ m^{-1} and $a = 51.4 \pm 9.71$ m^{-1}, respectively, obtained by applying equations
623 (S25a) and (S25b) in Supplemental Information) are also equal, within error, to the
624 inverse depth-scale estimated by Chandler et al. in their original publication ($a = 55$ m^{-1})
625 (Chandler et al., 2016). This inverse depth-scale corresponds to a "$1/e$-folding depth"
626 (i.e., the depth at which the E Profile's effective diffusivity declines to $1/e \approx 0.37$ of its
627 surficial value) of approximately 2 cm, which comports with field and laboratory
628 estimates for the thickness of the benthic biolayer (2 to 5 cm below the SWI) (Tomasek et
629 al., 2018; Knapp et al., 2017; Krause et al., 2017; Caruso et al., 2017; Trauth et al., 2014;
630 Harvey et al., 2013; Kessler et al., 2013; Zarnetske et al., 2011; Battin et al., 2008; Dahm
631 et al., 2002). Thus, turbulent mixing may play an outsized role in the biogeochemical
632 processing of nutrients and other contaminants in streambed and coastal sediments.

633 [Figure 7 goes about here]

634 While effective diffusivities inferred from data collected above and below the
635 SWI are strongly correlated, bias is evident for experiments with Permeability Reynolds
636 Numbers greater than the approximate threshold for a fully turbulent SWI, $\mathrm{Re}_K > 10^{0.3} = 2$
637 (Voermans et al., 2017) (**Figure 7a**). One possible explanation focuses on how Chandler
638 et al. measured Rhodamine concentrations in the interstitial fluids of the sediment bed.
639 Chandler et al.'s in-bed measurements of Rhodamine WT are taken at a "point" (sensing
640 volume ca., 0.23 cm^3) with fiber optic fluorometers, whereas our analytical framework

641 assumes that interstitial solute concentrations are horizontally averaged (**Section 2**).
642 Indeed, Chandler (2010) describes how measured time series of concentration in the
643 sediment were sensitive to fluorometer location and these differences appeared consistent
644 over time; i.e. tracer appeared to mix out of the streambed faster on one side of the tank
645 than on the other (ibid. pg. 173). These authors also document distinct and persistent
646 patterns of mean flow velocity within the tank (ibid. pg. 118) which would lead to
647 heterogeneous turbulence intensities and corresponding heterogeneous efflux across the
648 SWI at high Permeability Reynolds Numbers. To the extent that Chandler et al.'s point
649 measurements are not equal to horizontally averaged concentrations, the effective
650 diffusivities inferred from these data will suffer accuracy problems. Indeed, Chandler
651 (2010) noted an order of magnitude discrepancy in the timescale over which interstitial
652 Rhodamine WT concentration declined on opposite sides of the stirred tank—a
653 discrepancy that could induce order-of-magnitude inaccuracy in estimated sediment-side
654 diffusivities (the scale of disagreement seen in **Figure 7a**).

655 An alternative explanation is that the flux-gradient diffusive model (equation (1a))
656 is an imperfect descriptor of turbulent mass transfer in the interstitial fluids of the
657 sediment bed at high Permeability Reynolds Number—a conclusion supported by the
658 systematic loss of model performance (i.e., higher RMSE and lower AICc and R^2 values)
659 observed at large values of this dimensionless number (i.e., $\mathrm{Re}_K > 1$, **Figure 5**). Indeed,
660 the flux-gradient description of momentum transfer across other types of "porous"
661 boundaries, such as vegetation canopies, can break down; i.e., significant momentum flux
662 can occur in the absence of a velocity gradient, the analog of a concentration gradient for
663 mass transfer (Ghisalberti and Nepf, 2002). However, such observations typically occur

in the dispersive transport regime ($0.01 < \mathrm{Re}_K < 2$) where our estimates of effective diffusivity above and below the SWI are in general concordance (**Figure 7a**). It should also be noted that, even for the highest Permeability Reynolds Numbers trialed here and so long as the diffusivity is allowed to decay exponentially with depth, the flux-gradient diffusive model still explains a large fraction of variance in water column measurements of Rhodamine WT ($R^2 > 0.995$) (**Figure 5a**).

In summary, based on Chandler et al.'s laboratory measurements we can conclude the flux-gradient diffusive model is a reasonable representation of turbulent mass transfer in the interstitial fluids of the sediment bed*, provided that the vertical structure of the effective diffusivity is correctly specified (e.g., with the E Profile)*. However, a systematic loss of model performance is observed with increasing Permeability Reynolds Number in the turbulent diffusive regime ($\mathrm{Re}_K > 2$) possibly reflecting non-idealities associated with Chandler et al.'s experimental measurements, a more fundamental breakdown in the flux-gradient diffusive model, or some combination thereof. Further studies along these lines, particularly in field settings, are warranted.

5.3 Can Laboratory Measurements of Turbulent Mixing across the SWI be Extrapolated to Stream and Coastal Sediments?

Translation of these results to the field requires "scaling relationships" from which the E Profile's two parameters—the effective diffusivity and inverse depth-scale—can be estimated. Over the years a number of researchers have reported that effective diffusivities (inferred by fitting the C Profile's null model to flume measurements of turbulent mixing across flat sediment beds) exhibit a quadratic dependence on the Permeability Reynolds Number, $D_{\mathrm{eff},0}^{\mathrm{C}} \propto \mathrm{Re}_K^2$ (Richardson and Parr, 1988; O'Connor and

687 Harvey, 2008; Grant et al., 2012; Voermans et al., 2018; Grant et al., 2018). As noted
688 earlier, the Permeability Reynolds Number is calculated from the shear velocity, u_*,
689 sediment bed permeability, K, and the kinematic viscosity of water, υ. Permeability can
690 be estimated from the grain diameter and porosity of unconsolidated sediments (e.g.,
691 using the Kozeny-Carmen equation (Kamaan et al., 2007)) while the kinematic viscosity
692 of water is determined primarily by temperature (Rumble, 2019). Several methods are
693 available for measuring the shear velocity (c.f., Johnson and Cowen, 2017) including a
694 force-balance approach that provides spatially averaged estimates from the depth, h_w, and
695 slope, S [-], of a stream: $u_* = \sqrt{g h_w S}$ where $g = 9.81$ m s^{-2} is gravitational acceleration.
696 Thus, if the E Profile's two parameters can be expressed in terms of the Permeability
697 Reynolds Number, such relationships might pave the way for a direct translation of
698 laboratory measurements to field applications.

699 [Figure 8 goes about here]

700 When log-transformed effective diffusivities are plotted against the log-
701 transformed Permeability Reynolds Number, a significant change in slope and intercept
702 (as represented by non-overlapping 95% confidence intervals in equation (12a)) is
703 evident around $\mathrm{Re}_K = 1$ (**Figure 8a**).

704
$$\log_{10}\left(D^{\mathrm{E}}_{\mathrm{eff},0},\ \mathrm{m^2 s^{-1}}\right) = \begin{cases} \left(-5.31 \pm 0.09\right) + \left(2.53 \pm 0.17\right) \times \log_{10}\mathrm{Re}_K,\ R^2 = 0.905,\ \mathrm{Re}_K < 1 \\ \left(-5.57 \pm 0.06\right) + \left(0.99 \pm 0.15\right) \times \log_{10}\mathrm{Re}_K,\ R^2 = 0.440,\ \mathrm{Re}_K > 1 \end{cases} \quad (12a)$$

705 The power-law exponent for the surficial effective diffusivity declines from 2.53 ± 0.17
706 in the dispersive regime ($\mathrm{Re}_K < 1$) to 0.99 ± 0.15 in the turbulent diffusive regime
707 ($\mathrm{Re}_K > 1$). Likewise, the scaling behavior of the inverse depth-scale transitions from a

constant value ($a = 10^{1.74\pm0.01}$ m^{-1}) to a weak inverse dependence on the Permeability Reynolds Number ($a \propto \mathrm{Re}_K^{-0.32\pm0.08}$) (**Figure 8b**):

$$\log_{10}\left(a_E,\ \mathrm{m}^{-1}\right) = \begin{cases} 1.74\pm0.01,\ \mathrm{Re}_K < 1 \\ \left(1.69\pm0.02\right) - \left(0.32\pm0.08\right)\times\log_{10}\mathrm{Re}_K,\ R^2 = 0.18,\ \mathrm{Re}_K > 1 \end{cases} \quad (12b)$$

In the dispersive mixing regime ($\mathrm{Re}_K < 1$) the implied mixing depth, $1/a_E \approx 2$ cm, is between 4 and 130 times larger than the diameter of the glass spheres that make up the sediment bed ($0.150 \le d_g \le 5$ mm, depending on the experiment) and about 20 times larger than an estimate of the depth to which the time-averaged turbulent velocity boundary layer penetrates into the streambed called the Brinkman Layer thickness, $\delta_b \approx 20\sqrt{K} = 0.9$ mm (Voerman et al.'s 2017). It is also about ten-fold less than the depth of the sediment bed ($d_b = 20$ cm), implying that the inferred inverse depth scale is not a proxy for bed depth. These comparisons raise the question: *what is the physical interpretation of the inverse depth-scale?* Based on a model for mass exchange across the SWI by turbulent pumping, Higashino et al. (2009) reported that, at depths of around 2 cm and for shear velocities on the lower end of the range employed by Chandler et al. ($u_* = 0.01$ and 0.016 m s^{-1}), the root mean square vertical velocity of the interstitial pore fluids are >10% of their value at the SWI (ibid, Figure 3). Thus, one plausible interpretation is that the inverse depth-scale represents the surficial region of streambed over which tracer mass is vigorously mixed by turbulent pumping.

6 Conclusions

In this paper we developed and tested a rigorous one-dimensional modeling framework, based on Duhamel's Theorem, for predicting mass transfer across the SWI and in the

benthic biolayer of a turbulent stream. The framework allows for depth-varying diffusivity profiles, accounts for the change in porosity across the SWI, and encodes two-way coupling across the SWI, in which mass transfer into the water column from the sediment bed alters the water column concentration which, in turn, alters the mass flux from the water column to the sediment bed, and so on. We applied this theory to an extensive set of previously published measurements of turbulent mixing across a flat sediment bed in a closed stirred tank (Chandler et al., 2016) with the goal of evaluating the performance of four diffusivity depth profiles (C, E, E2M, and C2E Profiles). Key findings include: (1) the flux-gradient diffusive model is a reasonable representation of turbulent mass transfer across the SWI and in the interstitial fluids of the sediment bed, *provided that the vertical structure of the effective diffusivity is correctly specified*; (2) Chandler et al.'s experiments are most consistent with an exponentially declining diffusivity profile (i.e., the E Profile); (3) values of the E Profile's two parameters (effective diffusivity at the SWI, $D^{\mathrm{E}}_{\mathrm{eff},0}$, and inverse depth-scale, a_{E}) vary with the Permeability Reynolds Number, Re_K, a dimensionless number that incorporates bed shear stress and sediment permeability; (4) the dependence on the Permeability Reynold Number changes abruptly at $\mathrm{Re}_K = 1$, reflecting different modes of mixing below (turbulent dispersion, $D^{\mathrm{E}}_{\mathrm{eff},0} = 10^{-5.31\pm0.09}\mathrm{Re}_K^{2.53\pm0.17}$ and $a_{\mathrm{E}} = 10^{1.74\pm0.01}$) and above (turbulent diffusion, $D^{\mathrm{E}}_{\mathrm{eff},0} = 10^{-5.57\pm0.06}\mathrm{Re}_K^{0.99\pm0.15}$ and $a_{\mathrm{E}} = 10^{1.69\pm0.02}\mathrm{Re}_K^{-0.32\pm0.08}$) this threshold value; (5) the effective diffusivity's $1/e$-folding depth is approximately 2 cm, consistent with the hypothesis that solute mixing in the interstitial fluids of the sediment bed is facilitated primarily by turbulent pumping; and (6) this $1/e$-folding depth is also concordant with

751 field and laboratory measurements of the benthic biolayer thickness, implying that
752 turbulent mixing, and in particular turbulent pumping, may play an outsized role in the
753 biogeochemical processing of nutrients and other contaminants in streambed and coastal
754 sediments. Studies are presently underway to extend these findings to mixing across the
755 SWI by bedform pumping and bedform turnover with the ultimate goal of informing
756 pollutant fate and transport in coastal sediments and streams at catchment-to-continental
757 scales (Schmadel et al., 2019; Grant et al., 2018; Gomez-Velez et al., 2015; Gomez-Velez
758 and Harvey, 2014).

759 **Acknowledgments and Data**

760 The authors declare no conflicts of interest. All data used in this study are publicly
761 available (www.doi.org/10.15131/shef.data.10120205). SBG was supported by the U.S.
762 National Science Foundation (award 1840504), Virginia Tech's ICTAS EFO Opportunity
763 Seed Investment Grant, and the UC Office of the President Multi-campus Research
764 Program Initiative award (MRP-17-455083). JGV was funded by the U.S. National
765 Science Foundation (award EAR 1830172) and the U.S. Department of Energy, Office of
766 Biological and Environmental Research (BER), as part of BER's Subsurface
767 Biogeochemistry Research Program (SBR). This contribution originates from the SBR
768 Scientific Focus Area (SFA) at the Pacific Northwest National Laboratory (PNNL). IG
769 was supported by UK EPSRC Established Career Fellowship (award EP/P012027/1). MG
770 was funded by the Australian Research Council's Discovery Projects funding scheme
771 (DP120102500). KRR was supported by a fellowship from the Fulbright Program. JH
772 was supported by the USGS Water Resources Availability Program. SBG derived the
773 models and drafted the paper; IG compiled and contributed data; JGV, MG, IG, FB, KR,

774 and JH edited the manuscript, assisted with the interpretation of results, and contributed
775 text. Supporting Information includes a supplemental figure, tables and text. The authors
776 thank M. Chappell, A. Monofy, three anonymous reviewers, and the Associate Editor for
777 their insightful comments and manuscript edits.
778

References.

Aho, K., Derryberry, D., & Peterson, T. (2014), Model selection for ecologists: the worldviews of AIC and BIC. *Ecology*, 95(3), 631-636. doi:10.1890/13-1452.1

Azizian, M., Boano, F., Cook, P.L.M., Detwiler, R.L., Rippy, M.A., & Grant, S.B. (2017), Ambient groundwater flow diminishes nitrate processing in the hyporheic zone of streams, *Water Resources Research*, 53, doi:10.1002/2016WR020048.

Battin, T. J., Kaplan, L. A., Findlay, S., Hopkinson, C. S., Martí, E., Packman, A. I., et al. (2008), Biophysical controls on organic carbon fluxes in fluvial networks. *Nature Geoscience*, 1(2), 95–100. doi:10.1038/ngeo101

Boano, F., Revelli, R, & Ridolfi, L. (2011), Water and solute exchange through flat streambeds induced by large turbulent eddies. *J. Hydrol*ogy, 402, 290-296.

Boano, F., Harvey, J. W., Marion, A., Packman, A. I., Revelli, R., Ridolfi, L., & Wörman, A. (2014), Hyporheic flow and transport processes: Mechanisms, models, and biogeochemical implications. *Reviews of Geophysics*, 52, 603-679. doi:10.1002/2012RG000417

Bottacin-Busolin, A. (2019), Modeling the effect of hyporheic mixing on stream solute transport. *Water Resource Research*. 55, 9995-10011. doi: 10.1029/2019WR025697

Breugem, W. P., Boersma, B. J., & Uittenbogaard, R. E. (2006). The influence of wall permeability on turbulent channel flow. *Journal of Fluid Mechanics*, 562, 35–72.

Cardenas, M., J. L. Wilson, & R. Haggerty (2008), Residence time of bedform-driven hyporheic exchange. *Advances Water Research*, 31, 1382-1386.

Caruso, A., F. Boano, L. Ridolfi, D. L. Chopp, & A. Packman (2017), Biofilm-induced bioclogging produces sharp interfaces in hyporheic flow, redox conditions, and microbial community structure, *Geophys. Res. Lett.*, 44, 4917–4925, doi:10.1002/2017GL073651.

Chandler, I.D. (2012), "Vertical variation in diffusion coefficient within sediments", PhD thesis, Univ of Warwick, Coventry, U.K.

Chandler, I.D., Guymer, I., Pearson, J.M., & Egmond, R.V. (2016), Vertical variation of mixing within porous sediment beds below turbulent flows. *Water Resources Research*, 52, 3493-3509. doi.org/10.1002/2015WR018274

Dahm, C. N., Grimm, N. B., Marmonier, P., Valett, H. M., & Vervier, P. (2002), Nutrient dynamics at the interface between surface waters and groundwaters. *Freshwater Biology*, 40(3), 427–451. doi:10.1046/j.1365-2427.1998.00367.x

Elliott, A. H., & N. H. Brooks (1997a), Transfer of nonsorbing solutes to a streambed with bed forms: Theory, *Water Resources Research*, 33, 123–136.

Elliott, A. H., & N. H. Brooks (1997b), Transfer of nonsorbing solutes to a streambed with bed forms: Laboratory experiments. *Water Resources Research*, 33, 137–151.

Fleckenstein, J.H., Krause, S., Hannah, D.M., Boano, F. (2010), Groundwater-surface water interactions: New methods and models to improve understanding of processes and dynamics. *Adv. Water Resources*, 33, 1291-1295.

818 Franca, M.J. & Brocchini, M. (2015), Turbulence in Rivers. In P. Rowinski & A.
819 Radecki-Pawlick (Eds.), *Rivers—Physical, Fluvial, and Environmental Processes,*
820 GeoPlanet: Earth and Planetary Sciences, doi:10.1007/978030319-17719-9_2 (pp. 51–
821 78). Springer International Publishing, Switzerland.

822 Garcia, M.H. (2008), Sediment transport and morphodynamics, Sediment Engineering:
823 Processes, measurements, modeling, and practice. ASCE Manual No 110, Am. Soc. Of
824 Civ. Eng., ISBN 10 # 0784408149. doi:10.1061/40856(200)94

825 Ghisalberti, M., Nepf, H.M. (2002), Mixing layers and coherent structures in vegetated
826 aquatic flows. *J. Geophysical Research: Oceans*, 107, 3011. coi:10.1029/2001JC000871

827 Graf, U. (2004) "Applied Laplace Transforms and z-Transforms for Scientists and
828 Engineers—A Computational Approach using a Mathematica Package", New York, NY,
829 Springer-Basal AG, 1st Ed.

830 Grant, S. B. & Marusic, I. (2011), Crossing Turbulent Boundaries: Interfacial Flux in
831 Environmental Flows. *Environmental Science and Technology*, 45, 7107-7113.
832 doi:10.1021/es201778s

833 Grant, S. B. Stewardson, M. J. & Marusic, I. (2012), Effective diffusivity and mass flux
834 across the sediment-water interface in streams. *Water Resources Research*, 48, W05548.
835 doi:10.1029/2011WR011148

836 Grant, S. B., Stolzenbach, K., Azizian, M., Stewardson, M. J., Boano, F., & Bardini, L.
837 (2014), First-Order Contaminant Removal in the Hyporheic Zone of Streams: Physical
838 Insights from a Simple Analytical Model. *Environmental Science and Technology*, 48,
839 11369-11378. doi:10.1021/es501694k

840 Grant, S. B., Azizian, M., Cook, P., Boano, F. & Rippy, M. A. (2018a), Factoring stream
841 turbulence into global assessments of nitrogen pollution. *Science*, 359, 1266-1269.
842 https//doi:10.1126/science.aap8074

843 Grant, S.B. Gomez-Velez, J.D., & Ghisalberti, M. (2018b), Modeling the effects of
844 turbulence on hyporheic exchange and local-to-global nutrient processing in streams.
845 *Water Resources Research*, 54, doi:10.1029/2018WR023078.

846 Gomez-Velez, J. D., & Harvey, J. W. (2014), A hydrogeomorphic river network model
847 predicts where and why hyporheic exchange is important in large basins. *Geophysical*
848 *Research Letters*, 2014GL061099. doi:10.1002/2014GL061099

849 Gomez-Velez, J. D., Harvey, J. W., Cardenas, M. B., & Kiel, B. (2015), Denitrification in
850 the Mississippi River network controlled by flow through river bedforms. *Nature*
851 *Geoscience*, 8, 941-945. doi:10.1038/ngeo2567

852 Hall, R.O., Tank, J.L., Sobata, D.J., et al. (2009), Nitrate removal in stream ecosystems
853 measured by ^{15}N addition experiments: total uptake. *Limnology and Oceanography,* 43,
854 653-665.

855 Harvey, J. W., Böhlke, J. K., Voytek, M. A., Scott, D., & Tobias, C. R. (2013),
856 Hyporheic zone denitrification: Controls on effective reaction depth and contribution to
857 whole-stream mass balance. *Water Resources Research*, 49(10), 6298–6316.
858 doi:10.1002/wrcr.20492

859 Herzog, S.P., Higgins, C.P, Singha, K., & McCray, J.E. (2018), Performance of
860 engineered streambeds for inducing hyporheic transient storage and attenuation of
861 resazurin. *Environmental Science & Technology* 52, 10627-10636.

862 Hester, E. T., Cardenas, M. B., Haggerty, R., & Apte, S. V. (2017), The importance and
863 challenge of hyporheic mixing. *Water Resources Research*, 53(5), 3565–3575.
864 doi:10.1002/2016WR020005

865 Higashino, M.J., Clark, J., & Stefan, H. (2009) Pore water flow due to nearbed turbulence
866 and associated solute transfer in a stream or lake sediment bed. *Water Resources*
867 *Research* 45, W12414. doi:10.1029/2008WR007374

868 Hondzo, M. (1998), Dissolved oxygen transfer at the sediment-water interface in a
869 turbulent flow. *Water Resources Research,* 34(12), 3525-3533.

870 Iversen, N, & Jorgensen, B.B. (1993), Diffusion coefficients of sulfate and methane in
871 marine sediments: Influence of porosity. *Geochemica et Cosmochimica Acta*, 57, 571-
872 578.

873 Incropera, F.P., D.P. Dewitt, T.L. Bergman, & A.S. Lavine (2007), Fundamentals of Heat
874 and Mass Transfer, John Wiley, Hoboken, NJ.

875 Johnson, E.D., Cowen, E.A. (2017), Estimating bed shear stress from remotely measured
876 surface turbulent dissipation fields in open channel flows. *Water Resources Research*, 53,
877 1982-1996. doi:10.1002/2016WR018898

878 Kamann, P.J., Ritzi, R.W., Dominic, D.F., Conrad, C.M. (2007), Porosity and
879 permeability in sediment mixtures. *Ground Water* 45, 429-438.

880 Kessler, A.J., Glud, R.N., Cardenas, M.B., & Cook, P.L.M. (2013), Transport zonation
881 limits coupled nitrification-denitrification in permeable sediments. *Environmental*
882 *Science and Technology*, 47, 13404-13411.

883 Kim, T., Blois, G., Best, J., & Christensen, K. (2020). Experimental evidence of
884 amplitude modulation in permeable-wall turbulence. Journal of Fluid Mechanics, 887,
885 A3. doi:10.1017/jfm.2019.1027

886 Knapp, J.L.A., Gonzalez, Pinzon, R., Drummond, J.D., Larsen, L.G., Cirpka, O.A., &
887 Harvey, J.W. (2017), Tracer-based characterization of hyporheic exchange and benthic
888 biolayers in streams. *Water Resources Research*, 53, 1575-1594.
889 doi:10.1002/2016WR019393

890 Krause, S., Lewandowski, J., Grimm, N. B., Hannah, D. M., Pinay, G., McDonald, K., et
891 al. (2017), Ecohydrological interfaces as hot spots of ecosystem processes. *Water*
892 *Resources Research*, 53(8), 6359–6376. doi:10.1002/2016WR019516

893 Laube, G., Schmidt, C., & Fleckenstein, J.H. (2018), The systematic effect of streambed
894 conductivity heterogeneity on hyporheic flux and residence time. *Advances Water*
895 *Research,* 122, 60-69.

896 Leij, F.J., Priesack, E., Schaap, M.G. (2000), Solute transport modeled with Green's
897 functions with application to persistent solute sources. J. *Contaminant Hydrology* 41,
898 155-173.

899 Marion A., & M. Zaramella (2015) Diffusive behavior of bedform-induced hyporheic
900 exchange in rivers. *J. Environ. Eng.*, 131(9), 1260-1266. doi:10.1061/(ASCE)0733-
901 9372(2005)131:9(1260).

902 Myers, G.E. (1971), Analytical methods in conduction heat transfer, McGraw-Hill, New
903 York.

904 Nagaoka, H., & Ohgaki, S. (1990), Mass transfer mechanism in a porous riverbed. *Water*
905 *Research* 24(4), 417-425.

906 Newcomer, M.E., Hubbard, S.S., Fleckenstein, J.H., Maier, U., Schmidt, C., Thullner,
907 M., et al. (2016), Simulating bioclogging effects on dynamic riverbed permeability and
908 infiltration. *Water Resources Research*, 52(4), 2883-2900.
909 doi.org/10.1002/2015WR018351

910 O'Connor, B.L. & Harvey, J.W. (2008), Scaling hyporheic exchange and its influence on
911 biogeochemical reactions in aquatic ecosystems. *Water Resources Research*, 44,
912 W12423. doi:10.1029/2008WR007160

913 O'Connor, B.L., Harvey, J.W., & McPhillips, L.E. (2012), Thresholds of flow-induced
914 bed disturbances and their effects on stream metabolism in an agricultural river. *Water*
915 *Resources Research*, 48, W08504. doi:10.1029/2011WR011488

916 O'Connor, B.L., & Hondzo, M. (2008), Dissolved oxygen transfer to sediments by sweep
917 and eject motions in aquatic environments. *Limnology and Oceanography*, 53(2), 566-
918 578.

919 Packman, A.I., M. Salehin, M., & Zaramella, M. (2004), Hyporheic exchange with gravel
920 beds: Basic hydrodynamic interactions and bedform-induced advective flows. *ASCE J.*
921 *Hydraulic Engineeering.*, 130(7), 647-656.

922 Perez Guerrero, J.S., Pontedeiro, E.M. van Genuchten, M.Th., Skaggs, T.H. (2013),
923 Analytical solutions of the one-dimensional advection-dispersion solute transport
924 equation subject to time-dependent boundary conditions. *Chemical Engineering Journal*,
925 221, 487-491.

926 Pokrajac, D., & C. Manes (2009), Velocity measurements of a free-surface turbulent flow
927 penetrating a porous medium composed of uniform-size spheres, *Transp. Porous Med.*
928 78(3), 367–383, doi:10.1007/s11242-009-9339-8.

929 Pope, S.B. (2012), "Turbulent Flows", Cornell University, New York, U.S.A. doi:
930 10.1017/CB09780511840531

931 Reidenbach, M.A., Limm, M., Hondzo, M., & Stacey, M.T. (2010), Effects of bed
932 roughness on boundary layer mixing and mass flux across the sediment-water interface.
933 *Water Resources Research,* 46, W07530. doi:10.1029/2009WR008248

934 Richardson, C.P., & Parr, A.D. (1988), Modified Fickian model for solute uptake by
935 runoff. *ASCE J. Environmental Engineering*, 114, 792-809.

936 Roche, K.R., Blois, G., Best, J.L., Christensen, K.T., Aubeneau, A.F., & Packman, A.I.
937 (2018), Turbulence links momentum and solute exchange in coarse-grained streambeds.
938 *Water Resources Research*, 54, 3225-3242. doi:10.1029/2017WR021992

939 Roche, K.R., Li, A., Bolster, D., Wagner, G.J., & Packman, A.I. (2019), Effects of
940 turbulent hyporheic mixing on reach-scale transport. *Water Resources Research*, 55,
941 3780-3795.

942 Rumble, J. (Ed.) (2019) "CRC Handbook of Chemistry and Physics, 100th Ed." CRC
943 Press, Taylor and Francis Group, Boca Rotan, Florida.

944 Salehin, M., Packman, A.I., & Paradis, M. (2004), Hyporheic exchange with
945 heterogeneous streambeds: Laboratory experiments and modeling. *Water Resources*
946 *Research,* 40, W11504.

947 Schmadel, N.M., Harvey, J.W., Schwarz, G.E., Alexander, R.B., Gomez-Velez, J.D.,
948 Scott, D., & Ator, S.W. (2019), Small ponds in headwater catchments are a dominant
949 influence on regional nutrient and sediment budgets, *Geophysical Research Letters*,
950 46(16), 9669-9677. doi: 10.1029/2019GL083937

951 Stewardson, M.J., Datry, T., Lamouroux, N., Pella, H., Thommeret, N., Valette, L.,
952 Grant, S.B. (2016), Variation in reach-scale hydraulic conductivity of streambeds.
953 *Geomorphology*, 259, 70-80.

954 Thibodeaux, L.J., & Boyle, J.D. (1987), Bedform-generated convective transport in
955 bottom sediment. *Nature*, 325, 341-343.

956 Thibodeaux, L.J., Matisoff, G., Reible, D.D. (2011), "Bioturbation and Other Sorbed-
957 Phase Transport Processes in Surface Soils and Sediments", in *Handbook of Chemical*
958 *Mass Transport in the Environment* (L.J. Thibodeaux, D. Mackay, Eds.), CRC Press,
959 Taylor and Francis Group, Boca Raton, U.S.A.

960 Tomasek, A.A., Barman, T.D., Wang, P., Kozarek, J.L., Staley, C., Sadowsky, M.J., &
961 Hondzo, M. (2018). The effects of turbulence and carbon amendments on nitrate uptake
962 and microbial gene abundances in stream sediment. *J. Geophysical Research:*
963 *Biogeoscience*, 123, 1289-1301. https//doi:10.1002/2017JG004261

964 Trauth, N., Schmidt, C. Vieweg, M., Maier, U., & Fleckenstein, J. H. (2014), Hyporheic
965 transport and biogeochemical reactions in pool-riffle systems under varying ambient
966 groundwater flow conditions. *Journal Geophysical Research: Biogeosciences*, 119, 910-
967 928. https//doi:10.1002/2013JG002586

968 Voermans, J. J., Ghisalberti, M., & Ivey, G. N. (2017), The variation of flow and
969 turbulence across the sediment-water interface. *Journal of Fluid Mechanics*, 824, 413-
970 437. https//doi:10.1017/jfm.2017.345

971 Voermans, J. J., Ghisalberti, M., & Ivey, G. N. (2018), A model for mass transport across
972 the sediment-water interface. *Water Resources Research*, 54, 2799-2812.
973 https//doi:10.1002/2017WR022418

974 Weijs, S.V., Ruddell, B.L. (2020), Debates: Does Information Theory Provide a New
975 Paradigm for Earth Science? Sharper Predictions Using Occam's Digital Razor. *Water*
976 *Resources Research*, 56, e2019Wr026471. doi: 10.1029/2019WR026471

977 Wolke, P., Teitelbaum, Y., Deng, C., Lewandowski, J., Arnon, S. (2020), Impact of bed
978 form celerity on oxygen dynamics in the hyporheic zone. Water 12, 62.
979 https//doi.10.3390/w12010062

980 Wörman, A., (2000), Comparison of models for transient storage of solutes in small
981 streams. *Water Resources Research* 36(2), 455-468. doi:10.1029/1999WR900281

982 Zarnetske, J. P. Haggerty, R., Wondzell, S. M., & Baker, M. A. (2011), Dynamics of
983 nitrate production and removal as a function of residence time in the hyporheic zone.
984 Journal of *Geophysical Research: Biogeosciences*, 116(G1), G01025.
985 https//doi:10.1029/2010JG001356

986 Zheng, L., Cardenas M.B., Wang, L., & Mohrig, D. (2019) Ripple effects: bedform
987 morphodynamics cascading into hyporheic zone biogeochemistry. *Water Resources*
988 *Research,* Advanced online publication. https//doi:10.1029/29018WR023517

989 Zhong, Q., Chen, Q., Wang, H., Li, D., Wang, X. (2016), Statistical analysis of turbulent
990 super-streamwise vortices based on observations of streaky structures near the free
991 surface in the smooth open channel flow. *Water Resources Research*, 52, 3563–3578.
992 https//doi:10.1002/2015WR017728

Figure Captions.

Figure 1. (**a**) An illustration of how water column turbulence can influence mass transport in the benthic biolayer. In this diagram, the benthic biolayer consists of a flat coarse-grained streambed subject to turbulent pumping (traveling pressure wave, dashed blue line), turbulence penetration (red eddies), and a time-averaged turbulent velocity boundary layer that crosses the sediment-water interface (envelope of black arrows). The vertical mass flux $J(y)$ arising from these turbulence-linked phenomena is assumed to follow the flux-gradient diffusive model (equation (1a)). (**b**) Turbulent mixing across the SWI can be measured in the laboratory using closed systems, such as a stirred tank. Two-way coupling across the SWI is indicated by the two circular arrows.

Figure 2. Four functional forms of the effective diffusivity profile $f(y)$ trialed in this study (equations (8a) through (8d)). Variables represent the depth into the sediment bed (y), surficial effective diffusivity (at the SWI, $D_{\mathrm{eff},0}$), a mixing length-scale ($1/a$), and the thickness of enhanced mixing at the surface of the sediment bed (ℓ_t).

Figure 3. The influence of two-way coupling and finite bed depth on the evolution of solute concentration in the (**a**) water column and (**b**) interstitial fluids of the sediment bed, assuming solute is initially present only in the interstitial fluids of the sediment bed and the diffusivity profile is constant with depth (C Profile). See text for details.

Figure 4. Chandler et al.'s water (top panels) and sediment (bottom panels) column data compared to infinite bed model predictions for the **(a)** C Profile, (**b**) E Profile, and (**c**) C2E Profile. Black curves are model-predicted solute concentration in the water column (top panel) and at two depths in the sediment bed (15 and 151 mm below the SWI, lower panel). Blue horizontal lines represent the well-mixed (equilibrium) concentration (equation (9a)). Data highlighted in red correspond to Chandler et al.'s Exp ID 20110613.

Figure 5. Performance of the C, E and C2E infinite bed models across all 20 of Chandler et al.'s stirred tank experiments. Model performance metrics include: (**a**) coefficient of determination, R^2; (**b**) Root Mean Square Error, RMSE; and (**c**) Akaike's Information Criterion, AICc.

Figure 6. An evaluation of C2E fitting parameters inferred from Rhodamine concentration in the water column for all twenty of Chandler et al.'s stirred tank experiments. (**a**) Values of C2E's inverse depth scale vary over three orders of magnitude, as illustrated here with a violin plot. The effective diffusivity (**b**) and depth of the constant mixing zone (**c**) inferred from the C2E profile model (vertical axes) are strongly correlated ($R^2 = 0.93$ and 0.76) with, respectively, the E Profile's effective diffusivity and inverse decay depth-scale (horizontal axes).

Figure 7. A comparison of (**a**) effective diffusivities and (**b**) inverse depth-scales obtained by fitting the E Profile model to water column (vertical axis) or sediment column (horizontal axis) measurements of Rhodamine concentration. The points are colored to indicate the Permeability Reynolds Number.

Figure 8. Permeability Reynolds Number scaling of the E Profile's two parameters estimated from Chandler et al.'s water column measurements. The surficial diffusivity **(a)** and inverse decay length-scale (**b**) follow different scaling relationships in the dispersive (blue lines) and turbulent diffusive (green lines) ranges. Dashed curves are 95% prediction intervals.

1040 **Table 1.** Green's functions for various choices of the diffusivity depth profile and a finite
1041 or semi-infinite sediment bed.[1]

C Profile, $f_{\mathrm{C}}\left(\overline{y}\right)=1$
Semi-infinite Sediment Bed, $\overline{y}=a_{\mathrm{C}}y>0,\ \overline{s}=st_{\mathrm{T}}$
$\tilde{G}\left(\overline{y},\overline{s}\right)=e^{-\overline{y}\sqrt{\overline{s}}},\ \overline{y}>0$ (T-1)
Finite Sediment Bed, $\overline{y}=a_{\mathrm{C}}y>0$, $\overline{d}_b=d_b a_{\mathrm{C}}>0$, $\overline{y}<\overline{d}_b$, $\overline{s}=st_{\mathrm{T}}$
$\tilde{G}\left(\overline{y},\overline{s}\right)=\dfrac{e^{-\overline{y}\sqrt{\overline{s}}}\left(e^{2\overline{d}_{\mathrm{b}}\sqrt{\overline{s}}}+e^{2\overline{y}\sqrt{\overline{s}}}\right)}{1+e^{2\overline{d}_{\mathrm{b}}\sqrt{\overline{s}}}}$ (T-2)
E Profile, $f_{\mathrm{E}}\left(\overline{y}\right)=e^{-\overline{y}}$
Semi-infinite Sediment Bed, $\overline{y}=a_{\mathrm{E}}y>0$, $\overline{s}=st_{\mathrm{T}}$
$\tilde{G}\left(\overline{y},\overline{s}\right)=\sqrt{e^{\overline{y}}}\dfrac{K_1\left(2\sqrt{\overline{s}e^{\overline{y}}}\right)}{K_1\left(2\sqrt{\overline{s}}\right)}$ (T-3)
E2M Profile, $f_{\mathrm{E2M}}\left(\overline{y}\right)=\begin{cases} e^{-\overline{y}},\ 0\le\overline{x}\le\overline{\ell}_m \\ \overline{D},\ \overline{x}>\overline{\ell}_m \end{cases}$
Semi-infinite Sediment Bed, $\overline{y}=a_{\mathrm{E2M}}y>0$, $\overline{\ell}_m=-\ln\overline{D},\ 0<\overline{D}<1,\ \overline{D}=\dfrac{D'_{\mathrm{m}}}{D^{\mathrm{E2M}}_{\mathrm{eff},0}}$, $\overline{s}=st_{\mathrm{T}}$
$\tilde{G}\left(\overline{y},\overline{s}\right)=\begin{cases} \tilde{G}_1\left(\overline{y},\overline{s}\right),\ \overline{y}\le-\ln\overline{D} \\ \tilde{G}_2\left(\overline{y},\overline{s}\right),\ \overline{y}>-\ln\overline{D} \end{cases}$ (T-5a)
$\tilde{G}_1\left(\overline{y},\overline{s}\right)=\sqrt{e^{\overline{y}}}\dfrac{I_1\left(2\sqrt{e^{\overline{y}}\overline{s}}\right)\left[K_0\left(2\sqrt{\dfrac{\overline{s}}{\overline{D}}}\right)-K_1\left(2\sqrt{\dfrac{\overline{s}}{\overline{D}}}\right)\right]+K_1\left(2\sqrt{e^{\overline{y}}\overline{s}}\right)\left[I_0\left(2\sqrt{\dfrac{\overline{s}}{\overline{D}}}\right)+I_1\left(2\sqrt{\dfrac{\overline{s}}{\overline{D}}}\right)\right]}{K_1\left(2\sqrt{\overline{s}}\right)\left[I_0\left(2\sqrt{\dfrac{\overline{s}}{\overline{D}}}\right)+I_1\left(2\sqrt{\dfrac{\overline{s}}{\overline{D}}}\right)\right]+I_1\left(2\sqrt{\overline{s}}\right)\left[K_0\left(2\sqrt{\dfrac{\overline{s}}{\overline{D}}}\right)-K_1\left(2\sqrt{\dfrac{\overline{s}}{\overline{D}}}\right)\right]}$ (T-5b)
$\tilde{G}_2\left(\overline{y},\overline{s}\right)=\dfrac{e^{-\left(\overline{y}+\ln\overline{D}\right)\sqrt{\frac{\overline{s}}{\overline{D}}}}}{\sqrt{\overline{D}}}\dfrac{I_1\left(2\sqrt{\dfrac{\overline{s}}{\overline{D}}}\right)K_0\left(2\sqrt{\dfrac{\overline{s}}{\overline{D}}}\right)+I_0\left(2\sqrt{\dfrac{\overline{s}}{\overline{D}}}\right)K_1\left(2\sqrt{\dfrac{\overline{s}}{\overline{D}}}\right)}{K_1\left(2\sqrt{\overline{s}}\right)\left[I_0\left(2\sqrt{\dfrac{\overline{s}}{\overline{D}}}\right)+I_1\left(2\sqrt{\dfrac{\overline{s}}{\overline{D}}}\right)\right]+I_1\left(2\sqrt{\overline{s}}\right)\left[K_0\left(2\sqrt{\dfrac{\overline{s}}{\overline{D}}}\right)-K_1\left(2\sqrt{\dfrac{\overline{s}}{\overline{D}}}\right)\right]}$ (T-5c)
C2E Profile, $f_{\mathrm{C2E}}\left(\overline{y}\right)=\begin{cases} 1,\ 0\le\overline{y}\le\overline{\ell}_t \\ e^{-\overline{y}},\ \overline{y}>\overline{\ell}_t \end{cases}$
Semi-infinite Sediment Bed, $\overline{y}=a_{\mathrm{C2E}}y>0$, $\overline{\ell}_t=a_{\mathrm{C2E}}\ell_t>0$, $\overline{s}=st_{\mathrm{T}}$
$\tilde{G}\left(\overline{y},\overline{s}\right)=\begin{cases} \tilde{G}_1\left(\overline{y},\overline{s}\right),\ \overline{y}\le\overline{\ell}_{\mathrm{t}} \\ \tilde{G}_2\left(\overline{y},\overline{s}\right),\ \overline{y}>\overline{\ell}_{\mathrm{t}} \end{cases}$ (T-6a)

$$\tilde{G}_1\left(\bar{y},\bar{s}\right)=\frac{K_1\left(2\sqrt{\bar{s}}\right)\cosh\left[\sqrt{\bar{s}}\left(\bar{y}-\bar{\ell}_t\right)\right]-K_0\left(2\sqrt{\bar{s}}\right)\sinh\left[\sqrt{\bar{s}}\left(\bar{y}-\bar{\ell}_t\right)\right]}{K_1\left(2\sqrt{\bar{s}}\right)\cosh\left(\bar{\ell}_t\sqrt{\bar{s}}\right)+K_0\left(2\sqrt{\bar{s}}\right)\sinh\left(\bar{\ell}_t\sqrt{\bar{s}}\right)} \quad \text{(T-6b)}$$

$$\tilde{G}_2\left(\bar{y},\bar{s}\right)=\frac{e^{\left(\bar{y}-\bar{\ell}_t\right)/2}K_1\left(2e^{\left(\bar{y}-\bar{\ell}_t\right)/2}\sqrt{\bar{s}}\right)}{K_1\left(2\sqrt{\bar{s}}\right)\cosh\left(\bar{\ell}_t\sqrt{\bar{s}}\right)+K_0\left(2\sqrt{\bar{s}}\right)\sinh\left(\bar{\ell}_t\sqrt{\bar{s}}\right)} \quad \text{(T-6c)}$$

[1]The functions K_0 , K_1, and K_2 are Modified Bessel functions of the Second Kind, while I_0, I_1, and I_2 are Modified Bessel functions of the First Kind.

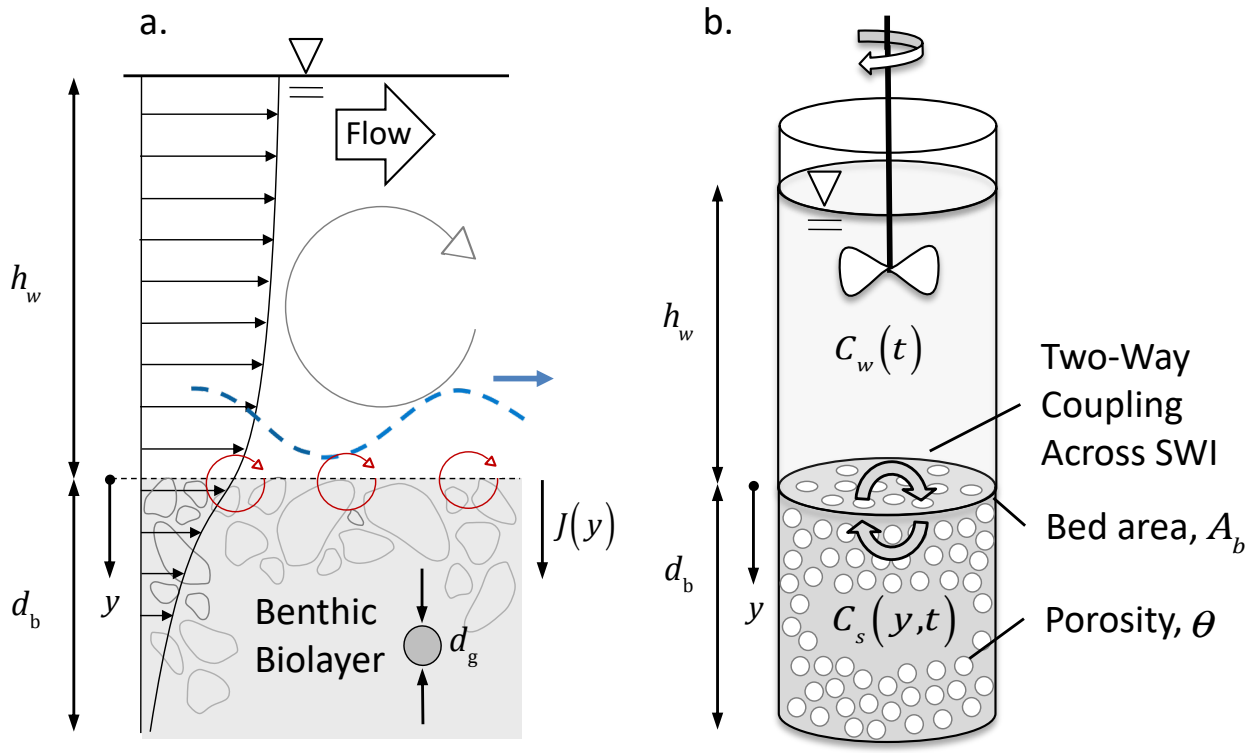

Figure 1. Grant et al. (2020)

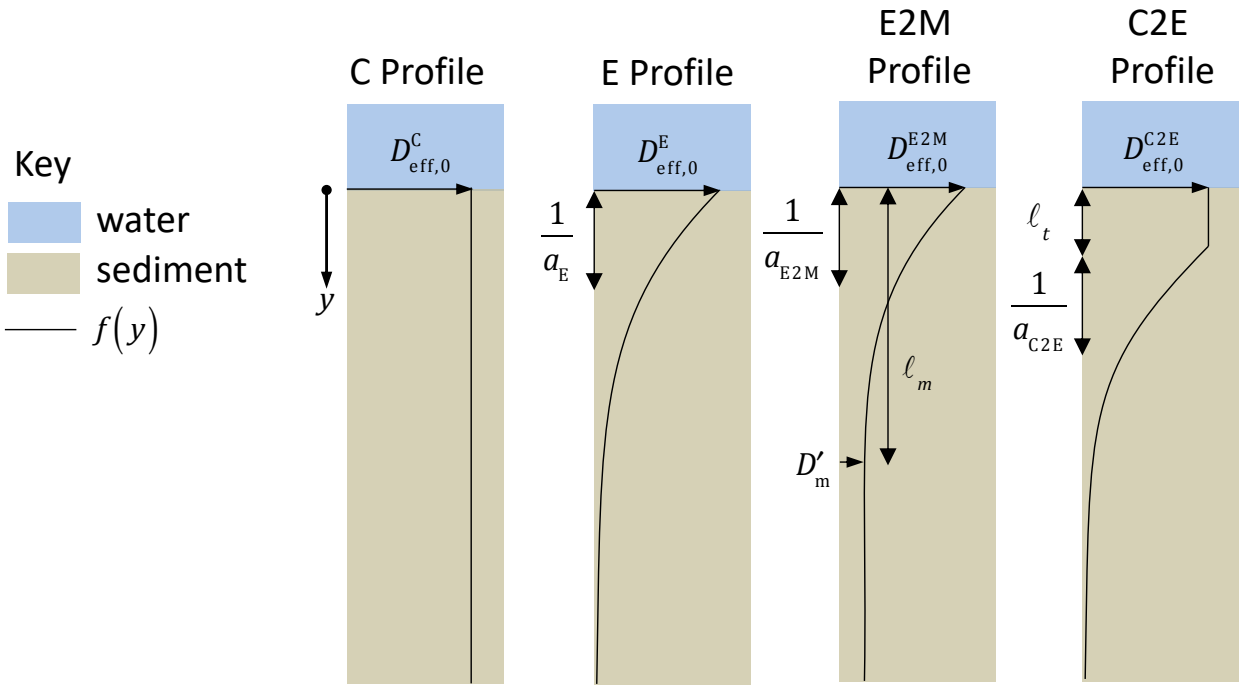

Figure 2. Grant et al. (2020)

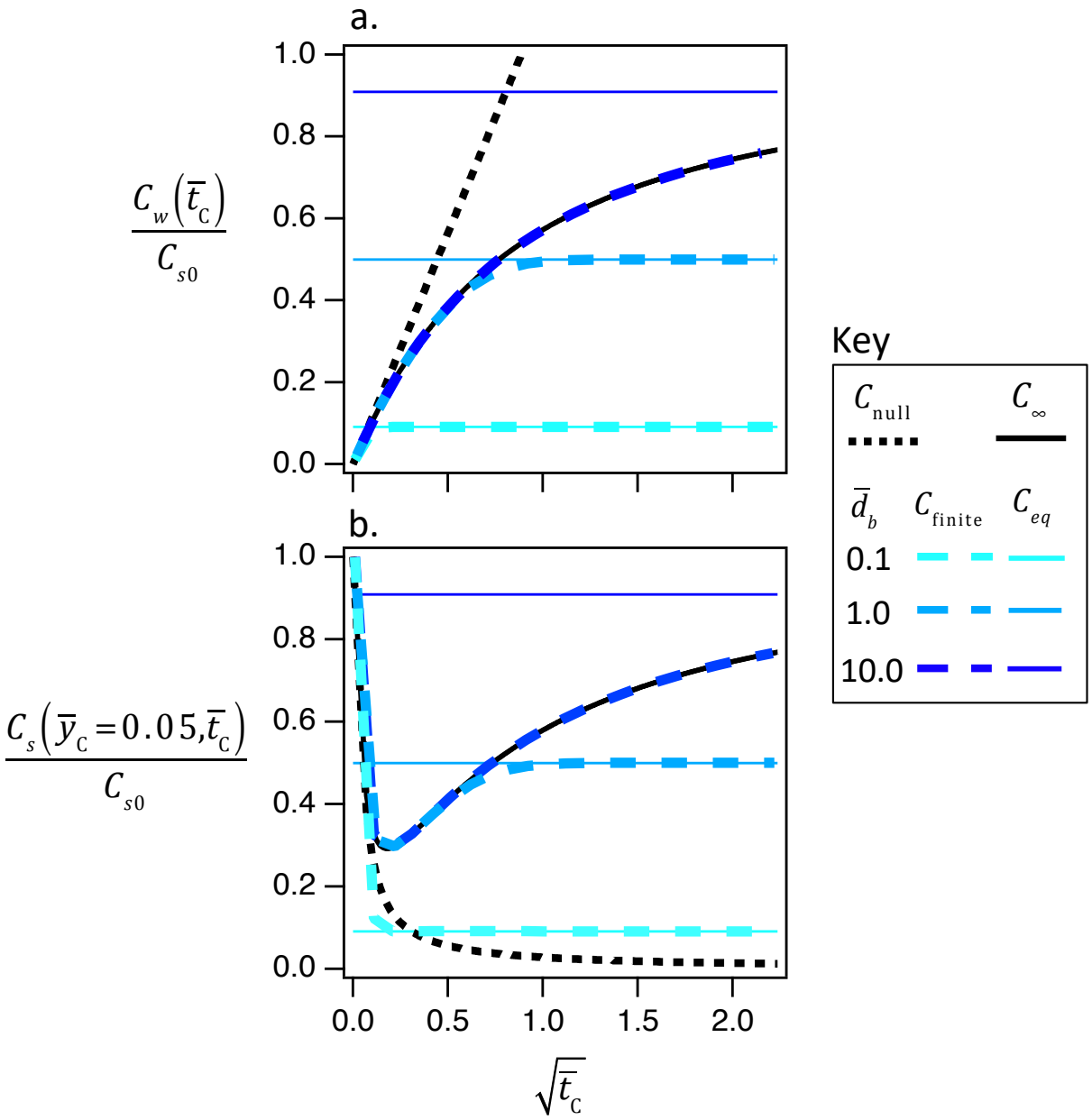

Figure 3. Grant et al. (2020)

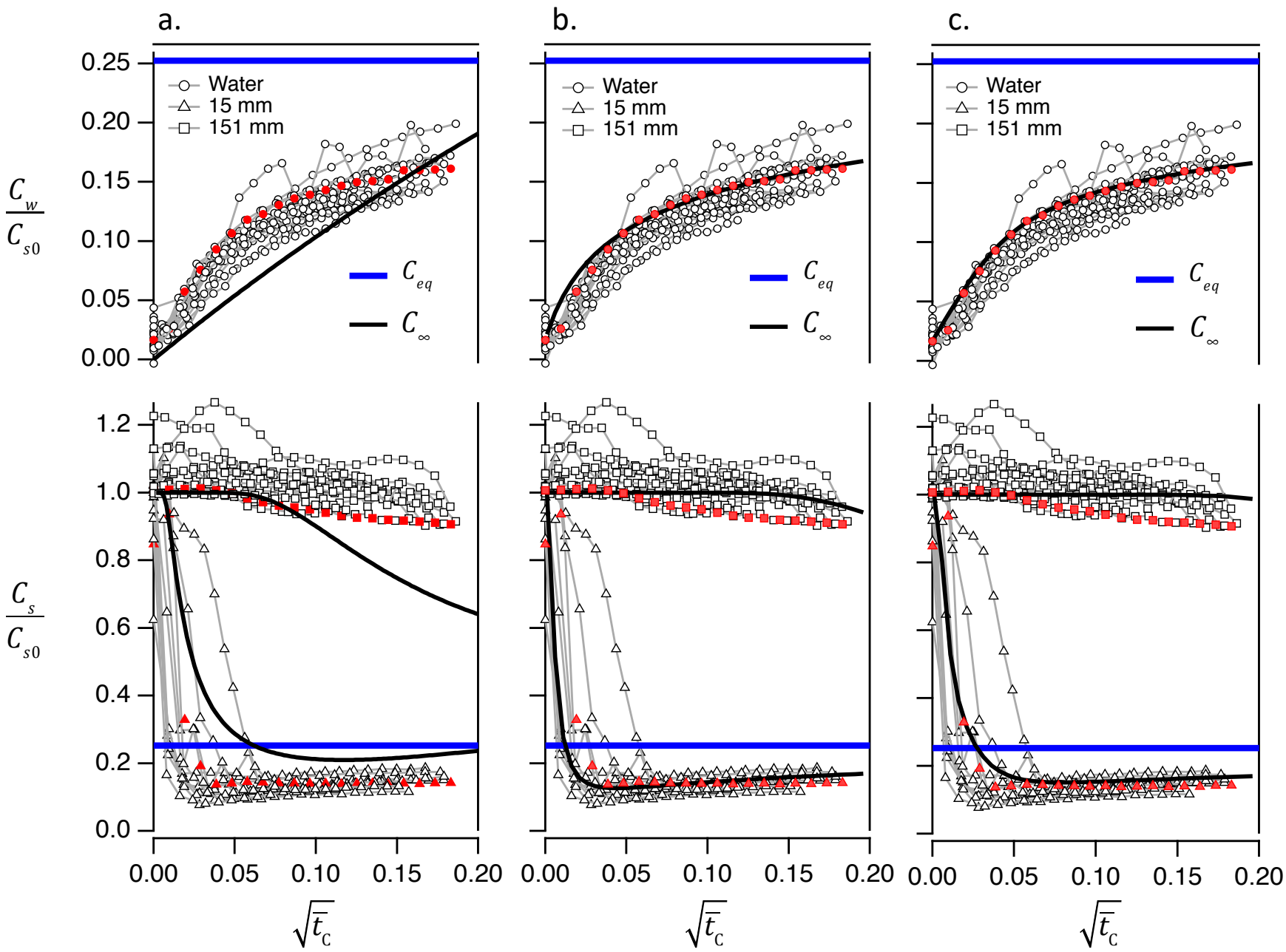

Figure 4. Grant et al. (2020)

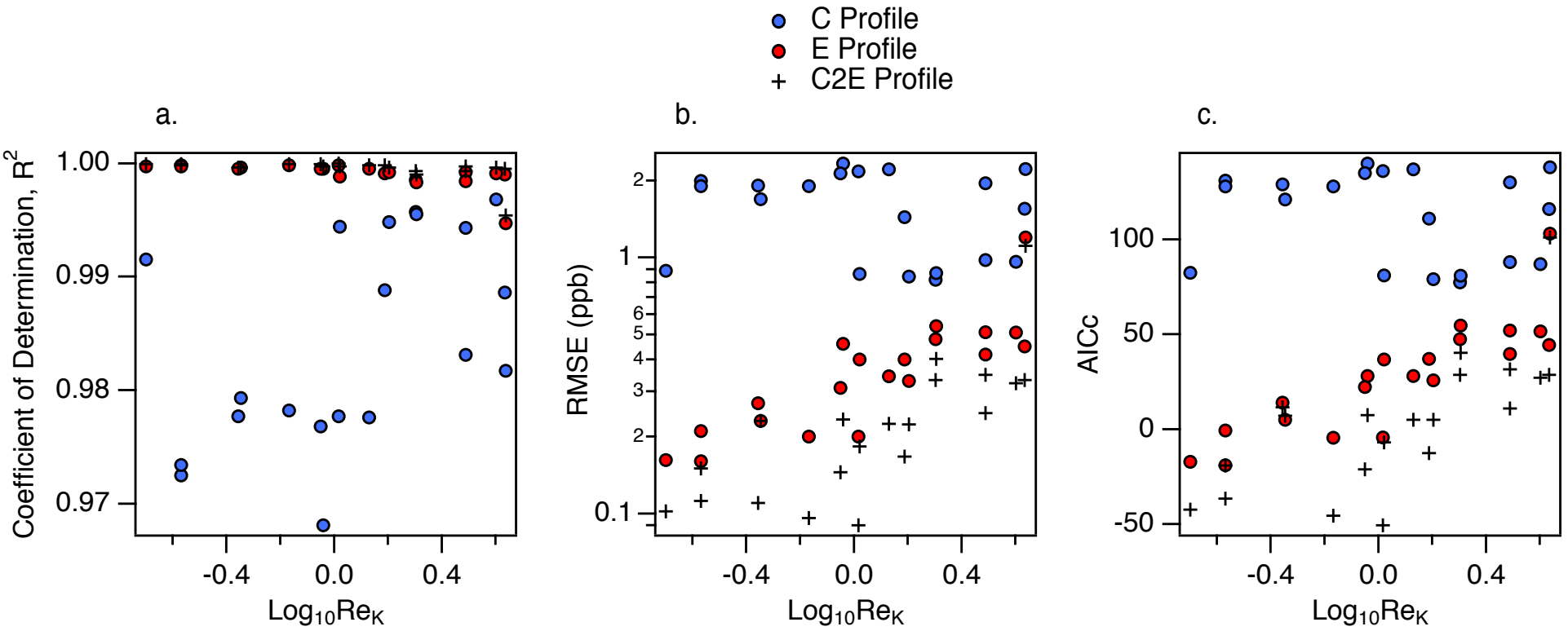

Figure 5. Grant et al. (2020)

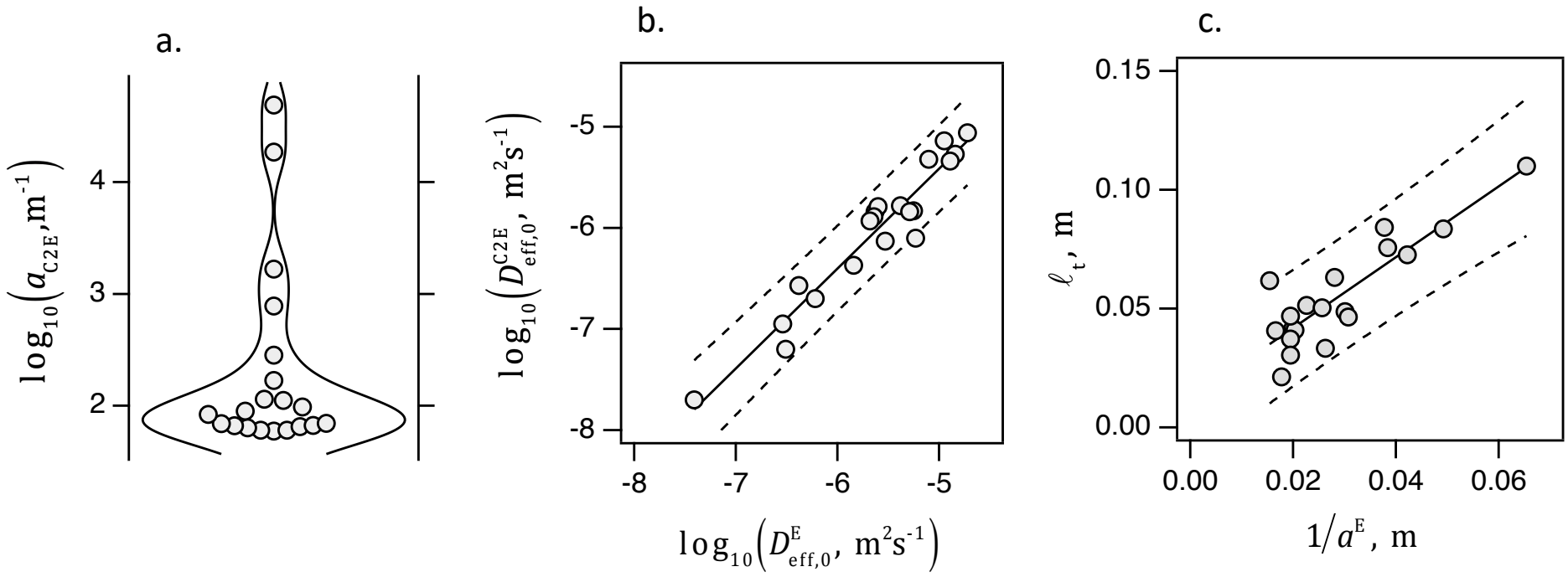

Figure 6. Grant et al. (2020)

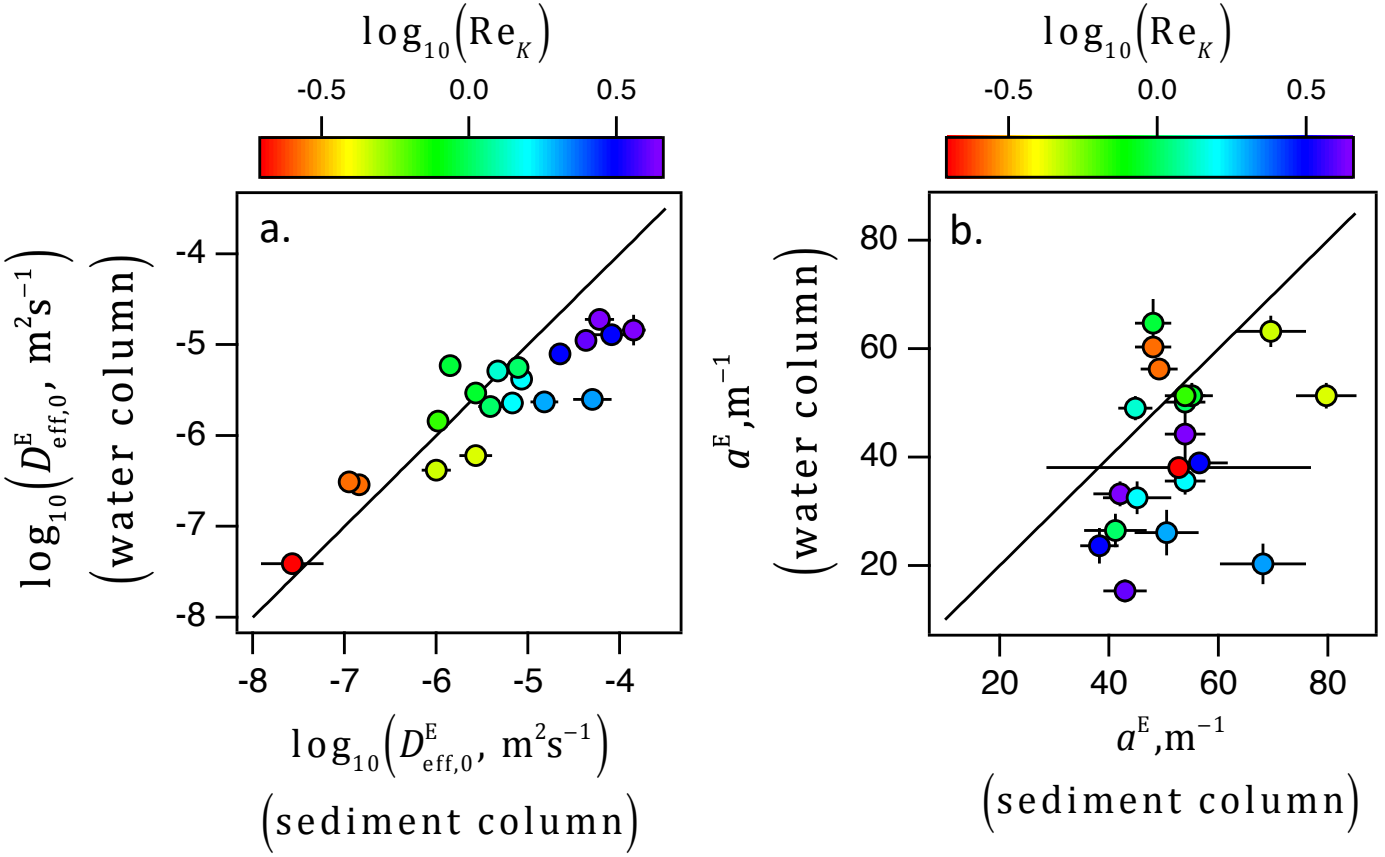

Figure 7. Grant et al. (2020)

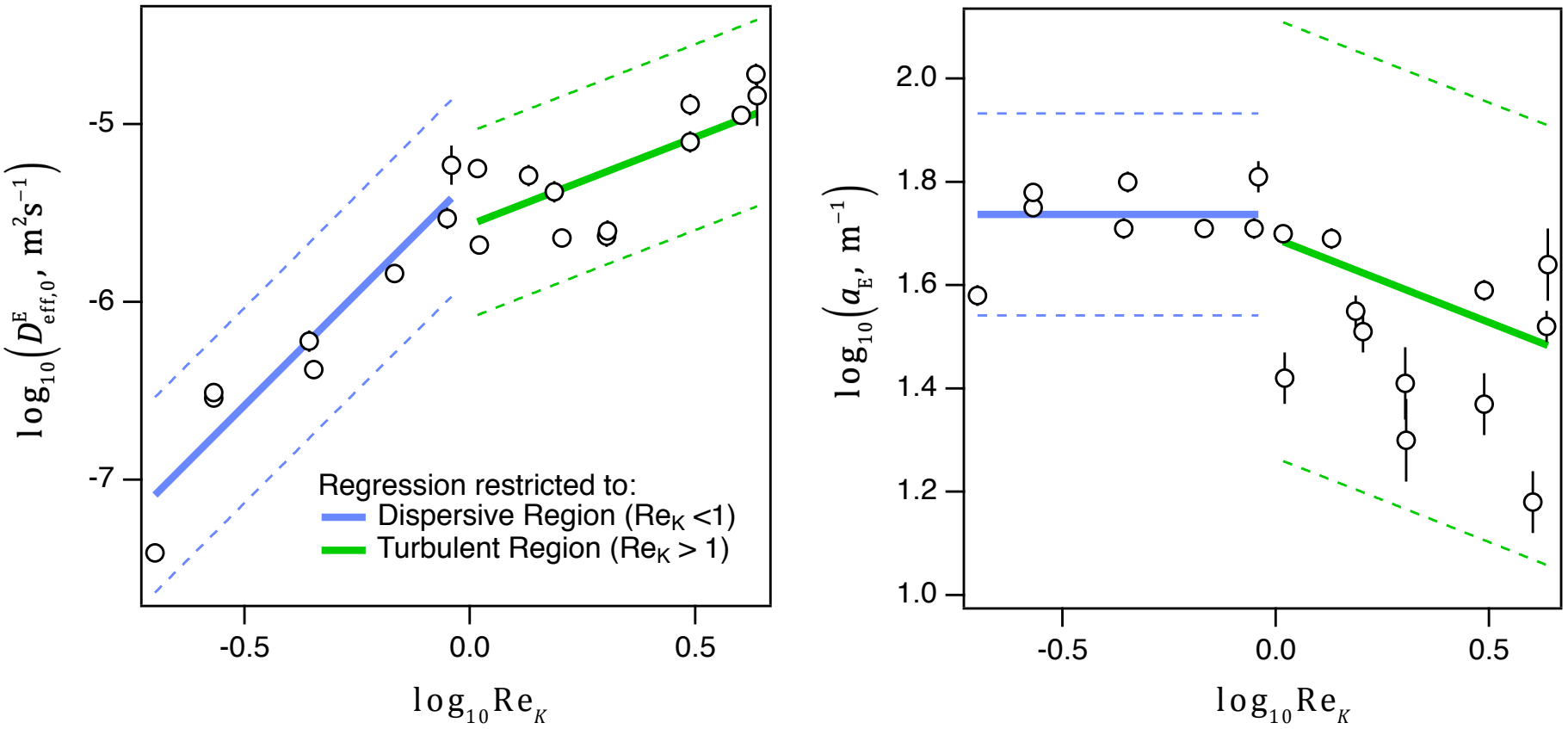

Figure 8. Grant et al. (2020)